Overview of the SCEC/USGS Community Stress Drop Validation Study Using the 2019 Ridgecrest Earthquake Sequence

Rachel E. Abercrombie*, Annemarie Baltay *et al.*

ABSTRACT

We present initial findings from the ongoing Community Stress Drop Validation Study to compare spectral stress-drop estimates for earthquakes in the 2019 Ridgecrest, California, sequence. This study uses a unified dataset to independently estimate earthquake source parameters through various methods. Stress drop, which denotes the change in average shear stress along a fault during earthquake rupture, is a critical parameter in earthquake science, impacting ground motion, rupture simulation, and source physics. Spectral stress drop is commonly derived by fitting the amplitude-spectrum shape, but estimates can vary substantially across studies for individual earthquakes. Sponsored jointly by the U.S. Geological Survey and the Statewide (previously, Southern) California Earthquake Center our community study aims to elucidate sources of variability and uncertainty in earthquake spectral stress-drop estimates through quantitative comparison of submitted results from independent analyses. The dataset includes nearly 13,000 earthquakes ranging from M 1 to 7 during a two-week period of the 2019 Ridgecrest sequence, recorded within a 1° radius. In this article, we report on 56 unique submissions received from 20 different groups, detailing spectral corner frequencies (or source durations), moment magnitudes, and estimated spectral stress drops. Methods employed encompass spectral ratio analysis, spectral decomposition and inversion, finite-fault modeling, ground-motion-based approaches, and combined methods. Initial analysis reveals significant scatter across submitted spectral stress drops spanning over six orders of magnitude. However, we can identify between-method trends and offsets within the data to mitigate this variability. Averaging submissions for a prioritized subset of 56 events shows reduced variability of spectral stress drop, indicating overall consistency in recovered spectral stress-drop values.

KEY POINTS

- We present initial findings from the 2019 Ridgecrest, California, sequence Community Stress Drop Validation Study.
- There is a substantial scatter in submitted spectral stress drops, both systematic and random, which we begin to disaggregate.
- Large-scale trends are method dependent, but relative between-event variation is more consistent.

Supplemental Material

INTRODUCTION

The seismic moment and stress release (or stress drop) during an earthquake are two of the most important parameters to characterize an earthquake rupture. The stress drop provides a measure of the stored elastic energy from geologic forces that is available during rupture to radiate as seismic waves, and the conditions under which an earthquake will continue to increase in size or trigger earthquakes nearby. It also strongly affects the high-frequency ground shaking, and so understanding how factors such as depth, strain rate, rheology, and scale affect stress release is fundamental to an improved understanding and modeling of the physics of earthquake rupture and future seismic hazards. Estimates of the stress drop can be derived from earthquake seismograms and spectra by making simplifying assumptions about the source, attenuation, and amplification of seismic waves as they travel through the earth. It has proved much harder to relate these measurements to the stress release on the fault, however making

Full author list and affiliations appear at the end of this article.

*Corresponding author: rea@bu.edu

Cite this article as Abercrombie, R. E., A. Baltay, S. Chu, T. Taira, D. Bindi, O. S. Boyd, X. Chen, E. S. Cochran, E. Devin, D. Dreger, *et al.* (2025). Overview of the SCEC/USGS Community Stress Drop Validation Study Using the 2019 Ridgecrest Earthquake Sequence, *Bull. Seismol. Soc. Am.* **115**, 734–759, doi: 10.1785/0120240158

"stress drop" possibly the most controversial parameter in earthquake science (refer to for example, Atkinson and Beresnev, 1997). Confusion over what the multitude of published estimates referred to as "stress drop" really represent, and how well they are resolved, and the lack of consistency between independent studies hampers research progress in a range of fields. For this reason, sponsored jointly by the U.S. Geological Survey (USGS) and the Statewide (previously, Southern) California Earthquake Center (SCEC) the SCEC/USGS Community Stress Drop Validation Study was designed and initiated (Baltay *et al.*, 2024), with the joint aims of enabling observational seismologists to improve their measurements and gaining understanding in the wider community of what those measurements really represent and how to use them. The initial focus has been on trying to obtain consistent measurements from the seismograms themselves, using the spectral methods most commonly applied to earthquakes that are too small or poorly recorded for detailed finite-fault inversion and individual study. Once there is more consistency in our measurements of the actual source radiation, the next step will be to investigate how these measurements relate to the true stress release on the fault and energy budget of the earthquake.

The overall goals of the Community Study as detailed in Baltay *et al.* (2024), are to:

1. Examine how different methods and assumptions contribute to variations in estimated spectral stress drop (hereafter referred to as spectral $\Delta\sigma$) and the prediction of high-frequency radiation. Do specific methods emphasize different frequency components of the earthquake source? How do data selection and preprocessing affect outcomes? What variations exist in how different analysts implement these methods?
2. Explore how variations in spectral $\Delta\sigma$ estimates reflect physical differences in earthquake source processes or material properties. Do simpler or smoother events exhibit greater agreement among spectral $\Delta\sigma$ estimates, whereas complex events exhibit more variability? How do these spectral $\Delta\sigma$ estimates correlate with factors like the earthquake's physical size, depth, location, or tectonic environment?
3. Develop best practices for reliably estimating spectral $\Delta\sigma$, to support ground motion and hazard modeling, and the broader community studying earthquake source physics and dynamic rupture processes (including laboratory investigations and numerical simulations). Although the optimal method for estimating spectral $\Delta\sigma$ may vary depending on factors such as tectonic context, inferred rheological properties, and rupture behavior, can we establish a foundational approach that ensures consistency across similar types of earthquakes?

The Community Study has been well supported internationally because is evident from the wide authorship of this article, which describes and presents the results submitted by over 20 independent groups. The waveform database (see the following Data section) remains online for future use to test and benchmark new methods. The reader is referred to the review by Abercrombie (2021) and the Community Study introduction and description by Baltay *et al.* (2024) for further information about the underlying limitations, and the priorities of the ongoing Community Study.

In this article, we present the results submitted in the first stage of the Community Study. All results submitted are included in the supplemental material, available to this article. We provide a brief description of the methods used, and the parameters assumed, and an initial analysis of the dataset as a whole. Many articles within this issue discuss individual or small groups of contributions and the effects of various methodological differences. Cochran *et al.* (2024), Mayeda *et al.* (2024), Shearer *et al.* (2024), and Abercrombie *et al.* (2025) perform more detailed analysis of subsets of events and methods to improve understanding of the systematic differences in the results obtained. Baltay and Abercrombie (2025) and Abercrombie and Baltay (2025) perform more detailed preliminary analyses of the overall dataset.

DATA

The common waveform database and associated metadata are described by Baltay *et al.* (2024), and are available for download at the Southern California Earthquake Data Center (see Data and Resources). The database uses relocated event locations from Trugman (2020) and preferred magnitudes (M) from the Southern California Seismic Network (SCSN) and consists of 12,943 earthquakes of M 1+ from two weeks from 4 July through 17 July 2019 (Fig. 1). This somewhat arbitrary time window was chosen to avoid any selection biases while ensuring a set of the larger aftershocks in the sequence. The dataset contains three M 5+ earthquakes and 86 M 4+ events in addition to the M 7.1 and 6.4 main earthquakes. Along with full waveform data from stations within 1° of the earthquake locations (Fig. 1b), we have provided phase picks and metadata, including the Trugman (2020) catalog with updated SCSN magnitudes (see Data and Resources). For more details on the waveform data including stations and processing details, please refer to Baltay *et al.* (2024).

To facilitate comparisons and allow more focused study, we selected a set of 56 earthquakes with SCSN catalog magnitudes (which are heterogeneous in type) ranging from 2 to 5.36. These events are well recorded and sample the main fault along strike and dip and do not show any correlation of depth with magnitude (Fig. 1d). We ask study participants to prioritize inclusion of these events in their analysis. We also identify eight events that can be used for very close comparison between the groups (labeled in Fig. 1a,c, and in Table 1); two of these are used by Shearer *et al.* (2024) for detailed investigation of separation of source and path components between methods; eight of the events in Table 1 (but not specifically the selected eight) are also part of a group of 18 moderate

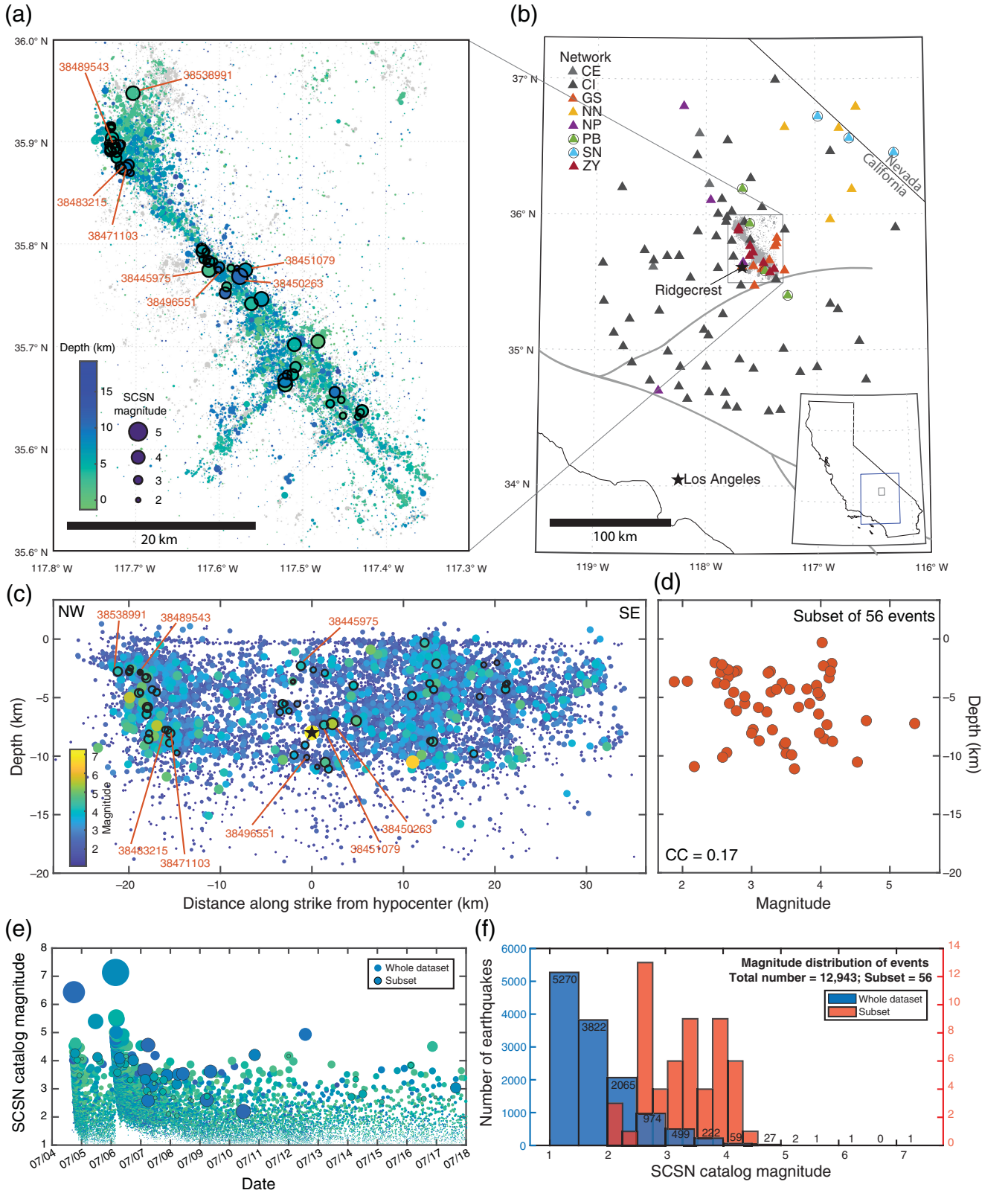

Figure 1. Distribution of earthquakes and stations used for the entire catalog (N = 12,943) and subset (N = 56) encircled by thick black lines. (a) Event map view of earthquakes colored by depth and sized by magnitude, with eight selected events labeled. (b) Station distribution colored by network (see Data and Resources). Temporary deployments (GS and ZY) shown outlined. Major southern California faults in gray, from the U.S. Geological Survey (USGS) Quaternary Faults database. Event-map location shown as small rectangle on inset map and station map as larger rectangle. (c) Cross section parallel to main M 7.1 strike, showing events with depth colored by magnitude, with selected eight events labeled. M 7.1 hypocenter given as black star. (d) Magnitude–depth scatter for the subset of 56 events showing no magnitude–depth bias. (e) Earthquake magnitude versus time, colored by depth as in panel (a). (f) Histogram of magnitude distribution for the entire catalog and subset of 56 events. (Figure partially adapted from Baltay *et al.*, 2024).

TABLE 1
Event Catalog for the Selected 56 Events

Event ID	Date (yyyy/mm/dd) Time (hh:mm:ss)	Longitude	Latitude	Depth (km)	Preferred Magnitude	Magnitude Type
38443535	2019/07/04 18:27:59	−117.54959	35.74649	6.989	4.66	M_w
38444103	2019/07/04 19:56:00	−117.52096	35.66316	2.099	4.16	M_w
38444215	2019/07/04 20:14:50	−117.50994	35.70201	4.844	3.99	M_{LR}
38445015	2019/07/04 22:02:35	−117.50862	35.68018	3.797	3.44	M_L
38445975*	2019/07/05 00:18:01	−117.61276	35.77449	2.301	4.04	M_w
38446071	2019/07/05 00:32:06	−117.48171	35.70511	0.309	4.02	M_w
38450263*	2019/07/05 11:07:53	−117.56916	35.76378	7.233	5.36	M_w
38451079*	2019/07/05 12:38:30	−117.56876	35.77477	7.34	4.09	M_w
38452095	2019/07/05 14:39:33	−117.56161	35.74187	3.975	3.94	M_w
38458071	2019/07/06 04:52:04	−117.73116	35.89079	5.839	3.68	M_{LR}
38458999	2019/07/06 06:34:47	−117.72287	35.89506	8.545	4.05	M_{LR}
38459327	2019/07/06 07:04:42	−117.72693	35.89476	6.415	3.97	M_w
38462063	2019/07/06 11:06:43	−117.62045	35.793	5.524	3.84	M_w
38462679	2019/07/06 11:53:08	−117.72927	35.89346	3.332	4.12	M_w
38464799	2019/07/06 15:09:15	−117.72392	35.88387	4.545	3.28	M_L
38466343	2019/07/06 17:41:33	−117.71332	35.8735	8.049	3.98	M_w
38466495	2019/07/06 17:59:14	−117.72936	35.90292	4.6	3.96	M_w
38469967	2019/07/07 01:05:07	−117.51197	35.6728	4.31	3.55	M_L
38470119	2019/07/07 01:23:55	−117.7313	35.91394	2.773	3.27	M_L
38470999	2019/07/07 03:13:12	−117.59315	35.7524	11.107	3.62	M_w
38471103*	2019/07/07 03:23:26	−117.71823	35.87326	7.778	3.3	M_L
38471847	2019/07/07 04:48:17	−117.60742	35.78274	5.536	2.9	M_L
38472279	2019/07/07 05:38:15	−117.57547	35.7687	10.53	4.53	M_w
38472295	2019/07/07 05:42:27	−117.707	35.8694	9.721	2.64	M_L
38472799	2019/07/07 06:44:44	−117.73076	35.91428	2.721	2.79	M_L
38474119	2019/07/07 09:09:25	−117.51871	35.67263	8.709	3.11	M_L
38474959	2019/07/07 10:32:54	−117.62112	35.79573	6.236	3.22	M_w
38475007	2019/07/07 10:37:45	−117.59139	35.75849	2.905	3.24	M_L
38475463	2019/07/07 11:29:31	−117.72984	35.91535	2.839	2.74	M_L
38478143	2019/07/07 17:44:09	−117.46704	35.64436	4.917	2.9	M_L
38478423	2019/07/07 18:19:19	−117.73146	35.89057	5.861	3.1	M_L
38479903	2019/07/07 21:02:51	−117.60037	35.77753	9.059	3.47	M_L
38480367	2019/07/07 22:18:19	−117.61461	35.78296	3.616	2.07	M_L
38481863	2019/07/08 01:57:20	−117.73312	35.89192	3.234	2.66	M_L
38483215*	2019/07/08 05:02:10	−117.71979	35.87579	7.751	3.02	M_L
38483263	2019/07/08 05:07:55	−117.61377	35.78422	3.659	1.88	M_L
38483591	2019/07/08 05:54:05	−117.7094	35.87715	8.876	3.49	M_L
38485391	2019/07/08 09:57:11	−117.46152	35.65567	9.79	3.5	M_w
38488519	2019/07/08 15:35:47	−117.73044	35.91308	2.484	2.61	M_L
38489543*	2019/07/08 17:30:03	−117.73407	35.89802	2.839	2.55	M_L
38496551*	2019/07/09 05:17:45	−117.60156	35.77464	10.117	2.58	M_L
38496647	2019/07/09 05:25:13	−117.72865	35.90127	4.564	2.74	M_L
38498615	2019/07/09 08:17:31	−117.61295	35.78317	9.909	3.58	M_w
38510015	2019/07/10 01:16:42	−117.45176	35.63268	2.02	2.47	M_L
38516455	2019/07/10 10:56:15	−117.57897	35.77654	10.918	2.17	M_L
38522647	2019/07/10 20:09:52	−117.52129	35.66736	8.76	4.17	M_w
38538991*	2019/07/11 23:45:18	−117.70418	35.9471	2.768	4.14	M_w
38562719	2019/07/14 02:28:17	−117.61611	35.79264	5.512	2.68	M_L
38564031	2019/07/14 06:06:39	−117.72388	35.88972	4.31	3.36	M_L
38565567	2019/07/14 11:46:11	−117.61972	35.78512	6.14	2.78	M_L
38570351	2019/07/15 03:12:42	−117.43357	35.6317	3.766	2.5	M_L
38577831	2019/07/16 02:47:05	−117.42888	35.63715	4.288	3.8	M_w
38580903	2019/07/16 13:16:17	−117.43058	35.63593	3.879	2.61	M_L
38583991	2019/07/16 22:38:43	−117.58615	35.77671	2.632	2.66	M_L
38587239	2019/07/17 09:46:06	−117.45381	35.6481	2.199	2.57	M_L
38589287	2019/07/17 15:07:21	−117.71873	35.8971	8.062	3	M_L

All locations (latitude, longitude, and depth) from relocations from Trugman (2020). Preferred magnitude and magnitude type from Southern California Seismic Network (SCSN) (see Data and Resources).

*Eight events denoted are highlighted for a more detailed study.

Ridgecrest earthquakes considered by Mayeda *et al.* (2024) to compare source parameters using four very different approaches, from coda analysis to finite-fault inversion.

In addition to the assembled waveforms, we also provide a processed ground-motion style flatfile database for the 56 target earthquakes and three additional M ≥ 5 earthquakes from the Ridgecrest sequence (supplemental material Datasets). This database includes ground-motion metrics: (1) peak ground acceleration (PGA), (2) peak ground velocity (PGV), (3) Fourier amplitude spectrum (FAS), and (4) pseudospectral acceleration (PGA %*g*). We used *gmprocess* (Thompson *et al.*, 2024a,b) software to analyze the waveforms from all available stations located within 100 km from the Ridgecrest mainshock. FAS and PSA were computed at 21 different periods from 0.01 to 10 s (0.1–100 Hz). The availability of this database should aid in ground-motion style analysis.

In the SCSN catalog, each event is assigned a preferred magnitude; local magnitude M_L is the preferred magnitude for most events smaller than about M 3.5, with moment magnitude preferred for larger events. Moment magnitude is commonly referred to as both **M** and M_w and here we use $M_w = 2/3\,(\log_{10}(M_0) - 9.05)$ (Hanks and Kanamori, 1979), with M_0 expressed in units of N·m. For moderate events in most of southern California, it has been observed that M_L is systematically larger than M_w, so an empirical correction factor was developed to yield the revised local magnitude, $M_{Lr} = M_L * 0.853 + 0.40125$ (SCSN catalog change history, Data and Resources). The main purpose of this is to bring the local magnitudes in line with moment magnitude for rapid response, and M_{Lr} is the initial preferred magnitude for M > 3.5 events. Within the SCSN catalog as a whole, M_{Lr} is usually replaced with M_w within a short time, but during dense aftershock sequences such as Ridgecrest, this is often not possible due to limitations of data quality (overlapping seismograms) and analyst time. For each of the 12,943 events considered in this dataset, the preferred catalog magnitude is thus moment magnitude for 102 events, local magnitude for 12,521, and revised local magnitude for 201 (119 events have neither a moment nor local magnitude).

Many of the spectral $\Delta\sigma$ methods, 42 of the 56 submissions, estimate an independent value of seismic moment, but others, such as spectral ratio methods, finite-fault inversions, or ground-motion-based methods, do not. For these submissions, we need a catalog-based seismic moment, and such a consistent moment value is also helpful for comparison between studies. Baltay and Abercrombie (2025) used the entire community dataset of submitted moments to develop a relationship between seismic moment (M_0) and local magnitude (M_L) specifically for the Ridgecrest dataset,

$$\log_{10}(M_0\mathrm{BA}) = 1.5M_L + 0.5\ln(1 + e^{4.6-M_L}) + 8.35, \quad (1)$$

(for M_0 in units of $\mathrm{N}\cdot\mathrm{m}$, and M_0BA means the moment is derived from M_L using the Baltay and Abercrombie, 2025, empirical relationship). Following Baltay and Abercrombie (2025), Table 1), we define study magnitudes and moments for consistency and ease of comparison:

Study catalog moment is from the SCSN preferred magnitude:

1. if the preferred catalog magnitude is M_w, then $\log_{10} M_0 = 1.5\ M_w + 9.05$;
2. if the preferred catalog magnitude is M_L, then M_0BA from equation (1).
3. if the preferred catalog magnitude is M_{Lr}, we first convert to M_L from: $M_{Lr} = M_L * 0.853 + 0.40125$, and then calculate M_0BA with equation (1).

Study catalog moment magnitude is directly derived from the adjusted catalog magnitude as $M_w\mathrm{BA} = (2/3)(\log_{10} M_0\mathrm{BA} - 9.05)$, in which again, M_0BA implies it is from the Baltay and Abercrombie (2025) regression relation. This prescription permits us to assign a unique magnitude per event, rather than having method-dependent magnitudes based on submitted moments.

We then incorporate the submitted moment magnitudes so that the study moment is preferentially the submitted moment, or the study catalog moment if no submitted moment is available; the study moment magnitude is $M_w = (2/3)(\log_{10} M_0 - 9.05)$ of the study moment. The study catalog values use seismic moment determined from the SCSN M_L using equation (1), whereas the study values use the respective submitted moment values where available, and the study catalog values when not (see Table S1 for definitions).

METHODS

The initial focus of the Community Stress Drop Validation study has been on spectral methods to analyze earthquakes that are mostly M < 5, but some methods include the larger earthquakes in the sequence. We have 20 unique groups submitting a total of 56 different results to date, with many groups submitting either variations of assumptions and analysis-selection assumptions in a single method or different methods, or both. The main methods are large-scale inversions (generalize inversion technique [GIT] and spectral decomposition), empirical Green's function (EGF) type spectral-ratio methods, those that solve for an independent exponential attenuation (Q or kappa function), finite-fault inversions, ground-motion-based methods, and other more individual approaches.

A recorded seismogram is a convolution of the source with propagation effects, typically divided between path (depending on travel time, or a function of distance or depth, between the source and receiver) and site, which is independent of the location of the earthquake, and here is taken to include the instrument response. Transforming to frequency, the recorded spectrum becomes simply the product of the source, path, and site terms. The different methods all involve selecting which time windows of which seismograms to analyze, attempting to

isolate the source component, and then finding the best-fitting source model to obtain the required source parameter estimates.

Once a source spectrum is determined, all methods fit a model to the displacement spectrum $u(f)$ of the form (Aki, 1967; Brune, 1970, 1971; Boatwright, 1980):

$$u(f) = \frac{\Omega_0}{\left[1 + \left(\frac{f}{f_c}\right)^{n\gamma}\right]^{1/\gamma}}, \quad (2)$$

to determine Ω_0, the long-period asymptote which is proportional to the seismic moment (Thatcher and Hanks, 1973), and f_c, the corner frequency, in which n governs the high-frequency fall-off rate and γ the shape of the corner. The Brune (1970) model is most commonly used, with $n = 2$ and $\gamma = 1$, whereas the Boatwright (1980) model has $n = 2$ and $\gamma = 2$. Other so-called double corner-frequency models are the superposition of two of these with two corner frequencies, one related to the source duration and the higher one related to a secondary process such as rise time, starting or stopping phases, or dynamic weakening (e.g., Denolle and Shearer, 2016). From the estimated f_c and study M_0, spectral $\Delta\sigma$ is then

$$\Delta\sigma = cM_0\left(\frac{f_c}{\kappa\beta}\right)^3, \quad (3)$$

with c a parameter related to the rupture geometry, taken to be 7/16 for a circular rupture (Brune, 1970), k a model parameter depending on the source model and phase analyzed (typical values are 0.2–0.3, e.g., Brune, 1970; Sato and Hirasawa, 1973; Madariaga, 1976; Kaneko and Shearer, 2015), and β the shear-wave velocity at the source. Refer to Cochran *et al.* (2024) for more discussion of spectral fitting.

There is some uncertainty as to whether these spectrally derived measurements represent a static or dynamic estimate of stress drop. At their simplest, they are a combination of an estimate of seismic moment with an estimate of source dimension, and hence slip, so perhaps are best thought of as estimates of an average static parameter, although depending on the nature of the underlying dynamic model. How closely they relate to the real stress change in the earth is an unsolved, and model-dependent question, so here we prefer to refer to them as "spectral" stress drops (spectral $\Delta\sigma$) for clarity and consistency.

To first get the earthquake source spectrum from the recorded seismogram, GIT methods attempt to decompose the spectrum into nonparameterized source, path, and site terms, and typically assume a reference or average site condition to remove terms common to all stations and events (e.g., Andrews, 1986; Oth *et al.*, 2011; Nakano *et al.*, 2015). Bindi *et al.* (2023a,b) demonstrate the trade-offs resulting from different analysis choices, including assumed attenuation and source models. The methods known as spectral decomposition (Shearer *et al.*, 2006) are similar, iteratively decomposing the spectra into relative source, path, and site terms. They differ from GIT methods primarily in that they typically use the same time window and frequency range for all events, and an estimated empirical correction spectrum (ECS) is used to map the resulting source spectra to an absolute scale. Shearer *et al.* (2019, 2022) developed improved methods of estimating the ECS, and other groups represented here prefer other variations.

The second most popular method type is EGF or spectral ratio. This is typically applied to smaller groups of earthquakes because the work is more intensive, and requires the existence of suitable EGFs. Abercrombie (2015) and Yoshimitsu *et al.* (2019) investigated how analysis choices could affect results. The EGF approach to isolate the source term is also used in finite-fault modeling (e.g., Dreger *et al.*, 2021).

In addition to these two most commonly used methods, a range of other approaches are in use. Many of these have overlapping assumptions and characteristics with one another and the two previous methods, or are simply a combination of methods, using one to constrain moment and the other to then determine corner frequency (e.g., Boyd *et al.*, 2017; Kemna *et al.*, 2021). Some start by estimating path-dependent attenuation (Q, t^*, or kappa) using a reference set of events (e.g., Calderoni *et al.*, 2019; Eulenfeld *et al.*, 2021); others invert the spectra to obtain best-fitting exponential attenuation and source models (e.g., Satriano *et al.*, 2016; Supino *et al.*, 2019).

We summarize all 22 methods submitted thus far to the Community Stress Drop Validation Study. Although overall we have 56 unique submissions, many are variations on the same theme. All methods are named starting with the name or initials of the authors, followed by an abbreviation for the method, and then wave types used (P, S, or both). The multiple variations published by Bindi *et al.* (2023a,b,c) are named differently to distinguish them. All the approaches share many underlying characteristics. Here, we simply refer the reader to previously published work or articles in this issue where relevant, and summarize the principal differences and assumptions in Figure 2. We include more detailed descriptions for those studies that are only published herein and do not have a separate reference. Each set of results has a consistent name, symbol, and color throughout the article, and these are included in Figure 2, in the legend to Figure 3, and in Figure S2 for easy reference.

Trugman (2020): Spectral decomposition

Trugman (2020) published one of the first analyses of source spectral parameters for earthquakes in the Ridgecrest sequence, using spectral decomposition of P waves following Trugman and Shearer (2017) and a spatially varying ECS. Study results name: Trugman_SpecDec_P.

Bindi, Zacarelli and Kotha (BZK) and Bindi *et al.* (2023a,b,c): GIT

Bindi *et al.* (2020) applied a GIT style spectral decomposition approach to compute the source parameters for earthquakes that occurred in the Ridgecrest region between 1999 and 2020 (Study

Method	Symbol	Name	Number of EQs	M range	Window length (s)	Omega n,γ	M_0	Q_d	Notes
GIT/spectral decomposition S		CUHK_SpecDec_S	4360	1-5.5 (*3.5)	3-10	2,1	Y	Y	>2 Hz only
		Chen_SpecDec1ECS_S	5905	1-5.5 (*3.5)	3	2,1	Y	N	1 ECS applied to all
		Chen_SpecDec1_2range_S	2811	1-5.5 (*3.5)	3	2,1	Y	Y	ECS calculated in 2 km depth ranges
		Chen_SpecDec1_75range_S	2799	1-5.5 (*3.5)	3	2,1	Y	Y	ECS calculated in 0.75 km depth ranges
		Devin_GIT_PS	52	2-5.5	Long	2,1	Y	N	
		Chu_SpecDec_S_good	208	2-5	4-10	2,1	N	N	
		SVF_SpecDec_S	3864	1.5-4.5 (*3.5)	1.5-4.5	2,1	Y	Y	ECS calculated within 2 km depth, 5 km epi. distance
		SVF_SpecDec1ECS_S	4125	1.5-4.5 (*3.5)	1.5-4.5	2,1	Y	N	1 ECS applied to all
		VSF_SpecDecPSn_S	4216	1.5-7 (*3.75)	1.3-2.6	1.8,1	Y	Y	ECS calculated within 2 km depth, 5 km epi. distance
		BZK_GIT_S	1996	1.8-7.1	≥8	2,1	Y	N	Attenuation travel time dependent, average site effect
GIT/spectral decomposition P		Trugman_SpecDec_P	11370	1.3-5 (*3.75)	2	2,1	Y	N	Epicentrally varying ECS
		SVF_SpecDec_P	5297	1.5-4.5 (*3.5)	1.5-4.5	2,1	Y	Y	ECS calculated within 2 km depth, 5 km epi. distance
		SVF_SpecDec1ECS_P	5753	1.5-4.5 (*3.5)	1.5-4.5	2,1	Y	N	1 ECS applied to all
		VSF_SpecDecPSn_P	6108	1-7 (*3.5)	1.3-2.6	2,1	Y	Y	ECS calculated within 2 km depth, 5 km epi. distance
		CUHK_SpecDec_P	3028	1-5.5 (*3.5)	3-10	2,1	Y	Y	>2 Hz only; ECS varies horizontally & with depth
Spectral ratio P		Abercrombie_SpecRatio_P	37	2.5-4.1	1-10	2,2	N	Y	Cross correlation ≥ 0.7 between EGF and target
		Huang_SpecRatio_P	13	2.5-4.1	1-4.2	2,2	N	Y	EGF within 3 ~source dimensions of target
Spectral ratio S		KemnaHarrington_SpecRatio_S	28	2.5-4.6	1-100	2,1	N	Y	
		Boyd_SpecRatio_coda	597	3.5-5.4	Long	2,1	Y	Y	EGF clusters within 5 km hypocentral distance, windows include direct S
		Chen_SpecRatio3s_S	747	1.5-5.5	3	2,1	N	Y	
		Chen_SpecRatio10s_S	538	1.5-5.5	10	2,1	N	Y	
		Chen_SpecRatioW10s_S	268	1.5-5.5	10	2,1	N	Y	
		Chen_SpecRatio5s_S	888	1.5-5.5	5	2,1	N	Y	
		Calderoni_SpecRatio_S	11	2.5-7.1	10-20	2,1	N	Y	
		Abercrombie_SpecRatio_S	22	2.6-4.7	1-10	2,2	N	Y	Cross correlation ≥ 0.7 between EGF and target
		Chu_SpecRatio_good_S	208	2.5-5	4-10	2,1	N	Y	

Figure 2. Summary of methods, and key to symbols in Figure 3 and subsequent figures. The Bindi *et al.* (2023a,b) comparative study symbols are grouped for simplicity, because detailed comparisons of these studies are already published. M_0 indicates whether the study submitted estimates of the seismic moment (yes/no), and Q_d indicates whether the method includes variability of path attenuation with source depth (yes/no). The SCSN magnitude range (M) is given, with * indicating a maximum M cut-off value applied for studies using short time windows (see Fig. 4). The omega square source model parameters are those of equation 2 (n, γ), and ? indicates it is a free variable. In the "Method" column where a range of time windows were used to calculate the spectra, the duration generally increases with magnitude and distance, especially if the whole waveform envelope is used; Long indicates windows of tens to hundreds of seconds, when there is no inherent problem with having insufficient low-frequency signal to resolve corner frequency and long-period asymptote for moment. Decon., deconvolution; ECS, empirical correction spectrum (applied in the spectral decomposition methods to account for average site effects); epi., epicentral; MRF, moment rate function; ref., reference; and κ, attenuation parameter. (*Continued*)

	★	DregerTaira_FF_PS	18	3.2-5.5	20	-	N	Y	EGF decon. recovers a coherent MRF at a station
	◆	Supino_SPAR_S	55	2-4.5	>=3	?,1	Y	Y	
	◆	Satriano_SourceSpec_S	55	2-4.5	5	2,1	Y	Y	
	■	Knudson_Amps_S	8263	1-5.5	3	2,1	Y	N	Narrowband filter time domain amplitudes
	■	Eulenfeld_Qopen_S	55	2-5.5	1-50	?,1	Y	N	
	◆	PBRT_Arias_PS	27	4.5-7.1	long	2,1	N	N	
	◆	KemnaHarrington_Qfit_S	31	3.4-5	1-100	?,1	Y	Y	
	■	KemnaHarrington_Stopping_S	26	3.3-4.7	-	-	N	Y	
	■	JiArchuleta_kappaE_S	42	4-5.4	2.8-5.8	2,1	N	N	
	◆	Calderoni_kappa_S	43	2.5-7.1	10-20	2,1	N	Y	κ from ref. events: 2 depth & 2 along strike bins.
	◆	Mayeda_CCT_coda	174	2.6-7.1	Long	2,1	Y	N	Windows start long after direct S
	■	Atkinson_GMM	78	3.6-7.1	Long	2,1	Y	N	
Bindi *et al.* 2023, GIT variations on a theme	+	d20_EPIH_AVE_BRUNEK	552	2.5-7.1	20	2,1	Y	Y	EPIH = attenuation depends on source depth HYPO = attenuation dependent on travel time only AVE = reference site is average of ALL stations SEL = reference site is selected stations
	+	d20_EPIH_SEL_BOAT	552	2.5-7.1	20	2,2	Y	Y	
	+	d20_EPIH_SEL_BRUNE	552	2.5-7.1	20	2,1	Y	Y	
	x	d20_HYPO_AVE_BRUNEK	556	2.5-7.1	20	2,1	Y	N	
	x	d20_HYPO_SEL_BOATW	556	2.5-7.1	20	2,2	Y	N	
	x	d20_HYPO_SEL_BRUNE	556	2.5-7.1	20	2,1	Y	N	
	+	d5_EPIH_AVE_BRUNEK	638	2.5-7.1	5	2,1	Y	Y	
	+	d5_EPIH_SEL_BOAT	638	2.5-7.1	5	2,2	Y	Y	
	+	d5_EPIH_SEL_BRUNE	544	2.5-7.1	5	2,1	Y	Y	
	x	d5_HYPO_AVE_BRUNEK	643	2.5-7.1	5	2,1	Y	N	
	x	d5_HYPO_SEL_BOAT	548	2.5-7.1	5	2,2	Y	N	
	x	d5_HYPO_SEL_BRUNE	643	2.5-7.1	5	2,1	Y	N	
	+	dv_EPIH_AVE_BRUNEK	469	2.5-7.1	5-20	2,1	Y	Y	
	+	dv_EPIH_SEL_BOAT	518	2.5-7.1	5-20	2,2	Y	Y	
	+	dv_EPIH_SEL_BRUNE	469	2.5-7.1	5-20	2,1	Y	Y	
	x	dv_HYPO_AVE_BRUNEK	522	2.5-7.1	5-20	2,1	Y	N	
	x	dv_HYPO_SEL_BOAT	522	2.5-7.1	5-20	2,2	Y	N	
	x	dv_HYPO_SEL_BRUNE	472	2.5-7.1	5-20	2,1	Y	N	

Figure 2. Continued

results BZK_GIT_S), with a further analysis by Bindi *et al.* (2021, results not included in study). Bindi *et al.* (2023a,b,c) investigated the effects of varying the assumptions concerning window length, attenuation structure, source model, and site correction underlying the spectral decomposition. Study results name: d20_EPIH_AVE_BRUNEK, and similar names (refer to Fig. 2).

Chen: Spectral decomposition and spectral ratios

Chen, Wu, and Pennington (2025) apply two methods: the first is three variations on a spectral decomposition approach with a single empirical correction, and two source-depth varying empirical corrections (following Chen and Abercrombie, 2020). Study results: Chen_SpecDec1ECS_S, Chen_SpecDec1_2range_S, and Chen_SpecDec1_75range_S. The second method is a spectral ratio approach, with a range of window length and empirical correction approaches. Study results name: Chen_SpecRatio3s_S, Chen_SpecRatio10s_S, Chen_SpecRatioW10s_S, and Chen_SpecRatio5s_S. For spectral ratio results, only events that have a valid seismic moment estimation from Chen_SpecDec1ECS_S and a time window, $n\,\mathrm{sec} = \mathrm{Round}(10 \times M_0^{1/3}/20{,}000)/10$

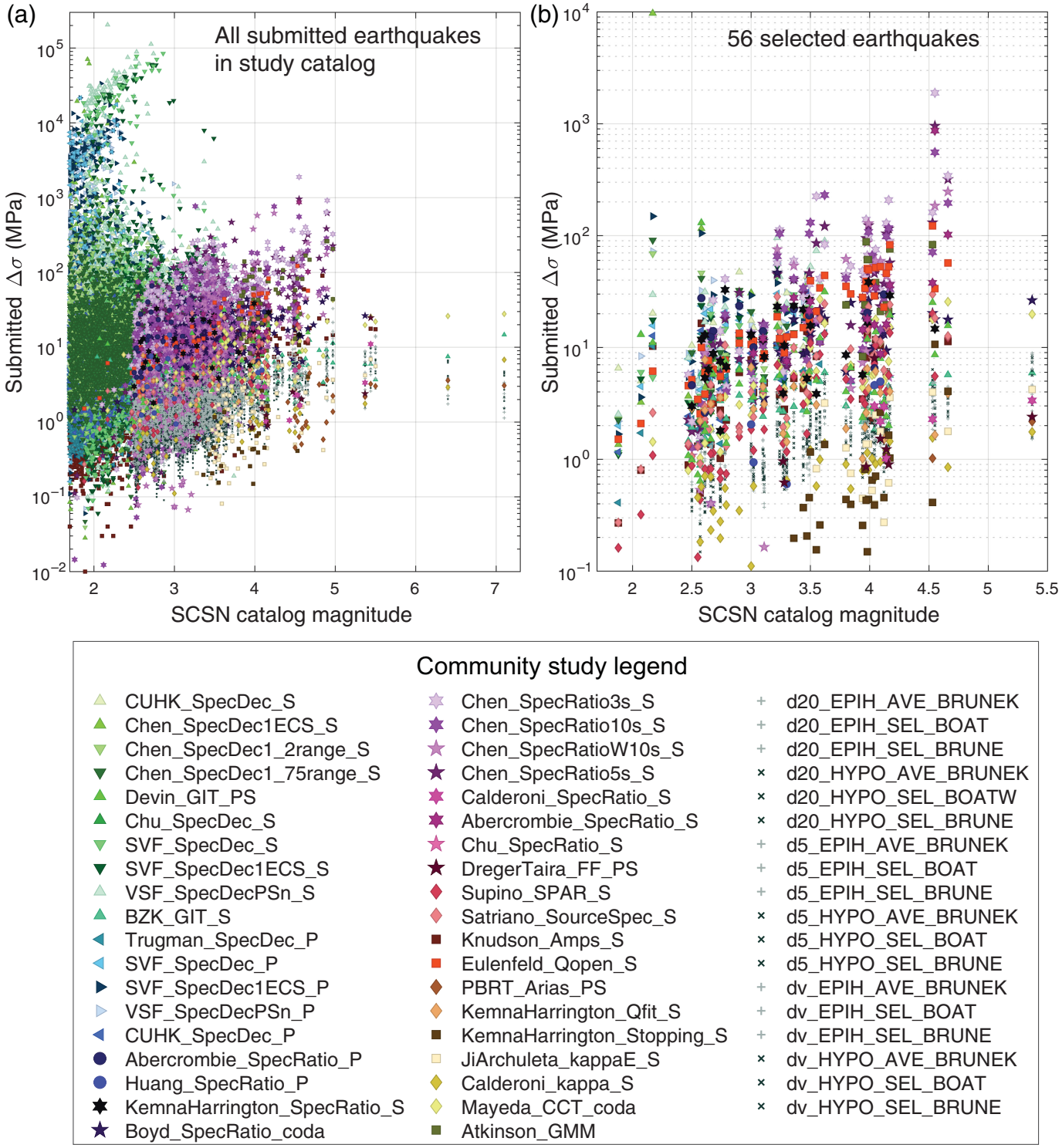

Figure 3. All submitted spectral $\Delta\sigma$-values in the Community catalog (Baltay *et al.*, 2024): (a) preferred Southern California Seismic Network (SCSN) catalog magnitude versus submitted stress drop for all submitted earthquakes; (b) the same for the 56 selected events (Table 1).

(Abercrombie *et al.*, 2017), shorter than 10 s are used. Note, the 3 and 5 s time windows may be too short for some events, but those results are still included for comparison. Chen, Yin, *et al.* (2025) further discuss the influence of time windows for spectral ratio analysis.

Devin: GIT

We apply the spectral decomposition/GIT developed by Andrews (1986) and furthered by Klimasewski *et al.* (2019). This method used separate data from the community provided waveforms, so we perform quality control (QC) and filtering of free-field earthquake waveforms using the USGS open-source software *gmprocess*, which includes default QC checks

(Thompson *et al.*, 2024a,b). For waveforms that pass, we remove the instrument response using stationXML files provided by network services, linear detrend and demean the records, apply a Hann taper with a width of 0.05, and band-pass filter using constant corner frequencies of 0.005 and 35 Hz. We window the waveforms with the start time chosen as the *P*-wave arrival using a travel-time calculation assuming the 1D velocity model of Kennett and Engdahl (1991), and the end time chosen using a significant duration model (Afshari and Stewart, 2016).

From these processed records, we compute power spectra (Prieto, 2022) for the two horizontal components individually, and then calculate the geometric mean, and resample in 75 evenly spaced log-frequency bins. We follow Klimasewski *et al.* (2019) to estimate source and site spectra including earthquakes with at least 10 records and stations that recorded at least three earthquakes. We include $1/R$ geometrical spreading and we assume that the effect of anelastic attenuation, Q, is negligible because our records are within 100 km of the source.

To constrain the amplitude of our inverted source and site spectra, we find the most Brune-like spectra in shape, if not amplitude, to use as a constraint function, following Klimasewski *et al.* (2019), unlike other GIT methods which use a reference site as a constraint. Finally, we estimate f_c and spectral $\Delta\sigma$ for each earthquake in our dataset by fitting Brune (1970) source models to each event spectrum, using nonlinear least squares with starting values of moment from the catalog, and starting values of f_c equal to the theoretical value at 5 MPa stress drop. Study results name: Devin_GIT_PS

Shearer, Vandevert, and Fan (SVF): Spectral decomposition

We apply the spectral decomposition approach described in Shearer *et al.* (2022) to both *P* waves and *S* waves. For the *P*-wave analysis, the ECS is computed by forcing the average corner frequency of M ∼1.5 earthquakes to 30 Hz, and Brune-model fits are performed from 2.5 to 35 Hz to estimate corner frequency and relative moment. For the *S*-wave analysis, the ECS is computed by forcing the average corner frequency of M ∼2 earthquakes to 14 Hz and fits are performed from 0.5 to 12 Hz. Two models each are provided for *P* and *S* waves, one in which a single ECS spectrum is computed for the entire dataset ("1ECS" in model label) and one in which spatially varying ECS spectra are computed from the small earthquakes within 2 km in depth and 5 km horizontally. Study results names: SVF_SpecDec_P, SVF_SpecDec1ECS_P, SVF_SpecDec_S, and SVF_SpecDec1ECS_P.

Vandevert, Shearer, and Fan (VSF): Spectral decomposition

Vandevert *et al.* (2024) apply a further variation of the spectral decomposition approach, with the following differences from the SVF models: (1) the spectra are computed using a Hann taper rather than multitapers, which makes the spectra rougher but more reliable at very low frequencies; (2) the *S*-wave reference average corner frequency is 17 Hz for M 2 earthquakes and the high-frequency fall-off rate is 1.8. These changes were made to provide a better agreement of the *S*-wave spectral $\Delta\sigma$ estimates with the *P*-wave estimates; and (3) only models based on the spatially varying ECS function are provided. Study results name: VSF_SpecDecPSn_P and 12_VSF_SpecDecPSn_S.

Chu: Spectral decomposition and spectral ratio

We apply two methods for which the preprocessing and initial spectra are identical: a spectral ratio approach, described in Chu *et al.* (2025), and a spectral decomposition method (refer to Trugman and Shearer, 2017; Shearer *et al.*, 2006, for more background on this method; refer to Vandevert *et al.*, 2024, for similar methodologies; Chen, Wu, and Pennington, 2025).

In this application of the spectral decomposition approach, a station is required to record a minimum of eight events, and an event is required to be observed at a minimum of eight stations, to be included in the inversion. The path is binned by 20 evenly spaced travel-time bins between 0 and 30 s, and at each frequency point, we solve for relative inverted spectra for the event, station, and travel path (as defined by travel time) using an iterative least-squares solver. We then use a self-organizing map algorithm to split the data into six spatial clusters and for each cluster, we compute an ECS by first binning and stacking the events into magnitude bins with edges at [2.2, 2.4, 2.6, 2.8, 3.0, 3.2, 3.4, 3.6, 3.8] and constraining the lowest magnitude bin of events to fit a Brune model, while performing a grid search over stress drop (refer to Shearer *et al.*, 2006; Chen and Abercrombie, 2020). We then choose the ECS that yields the lowest misfit to correct all magnitude bins. Although our clustering does not include any depth constraints because the average depth of the clusters differs, there is some inherent adjustment for gross variations in source depth. Study results name: Chu_SpecRatio_good_S (spectral ratio) and Chu_SpecDec_S_good (spectral decomposition).

Zhang and Yang (CUHK): Spectral decomposition

Zhang and Yang (2025) apply the refined spectral decomposition approach named "Differential-Evolution-based Spectral Correction" following Zhang *et al.* (2024), to both *P* and *S* waves independently. Study results name: CUHK_SpecDec_P and CUHK_SpecDec_S.

Supino: Attenuation model

We invert single-station *S*-wave displacement spectra to estimate source parameter seismic moment M_0 and corner frequency f_c. We use the probabilistic approach proposed by Supino *et al.* (2019), with the same data preprocessing described therein. We use a theoretical Green's function with a free parameter Q' modeling the anelastic attenuation along the source-station

path (Supino *et al.*, 2024). The single-station solution is the joint a posteriori probability density function $\sigma(m = \log M_0, f_c, n)$, conditional on the Q'-value that minimizes the misfit function. The event solution is, for each parameter, the weighted average of single-station marginal means, in which the weight is the inverse of the corresponding marginal variance.

To account for station site effects, we follow a two-step approach. In the first step, we estimate the site-effect term by averaging frequency-by-frequency, at each station and for all the events in the dataset, the residuals between the observed spectrum and the event solution spectrum. In the second step, we invert the single-station spectra corrected for the corresponding site-effect term. Study results name: Supino_SPAR_S.

Satriano: Attenuation model

We use SourceSpec (v.1.8, Satriano *et al.*, 2016; Satriano, 2024) to determine the earthquake source parameters (M_0, f_c) and inelastic attenuation (t^*) by the modeling of *S*-wave displacement spectra. The *S*-wave spectrum at a given station is computed from the vector sum of Fourier amplitude spectra from the three displacement components using a 5 s time window starting 0.5 s before the *S*-wave arrival. The displacement spectrum is converted into moment units using an *S*-wave velocity of 3500 m/s, a density of 3000 kg/m^3, an average radiation pattern coefficient of 0.63, a free-surface term of 2, and a body-wave geometrical spreading correction (e.g., Thatcher and Hanks, 1973). The spectrum is then smoothed with a 0.2-decade wide window and linearly resampled in log-frequency space to prevent overfitting at high frequencies. The same procedure is applied to construct the noise spectrum, using a window between 7 and 2 s before the *P*-wave arrival.

Each station is analyzed individually, and the best-fitting spectral model is obtained by grid search, with the misfit function defined as the root mean square (rms) of the differences between the observed and modeled spectra between 0.1 and 40 Hz, weighted by the signal-to-noise ratio (SNR).

Event-averaged source parameters are generated from the median values of the single-station parameters, with uncertainties represented by the 15.9th and 84.1st percentiles (equivalent to ±1 sigma for a Gaussian distribution). A theoretical summary spectrum is constructed from the summary estimates of M_0, f_c, and t^*, and station residuals are calculated as the differences between the observed and the summary spectra. Mean station residuals are computed at each station by averaging all event-based residuals. These mean station residuals accounting for site-specific effects such as resonances or high-frequency spectral decay are then used to correct the measured spectra in a second run of SourceSpec. Study results name: Satriano_SourceSpec_S.

Knudson: Attenuation model

Knudsen *et al.* (2025) obtain their initial spectra from the peak-amplitude narrowband-pass-filtered seismograms, and then apply an inversion method based on that of Al-Ismail *et al.* (2023). Study results name: Knudson_Amps_S.

Eulenfeld: Attenuation model

We apply the Qopen method (Eulenfeld and Wegler, 2016; Eulenfeld *et al.*, 2021, 2023) to the 56 selected events (Table 1), assuming an average shear-wave velocity of 3200 m/s and a bulk density of 2700 kg/m^3. Qopen first fits observed seismic envelopes (energy density) of the shear-wave onset and coda with a synthetic Green's function accounting for scattering, intrinsic attenuation, and geometrical spreading, as well as source and site terms, before modeling the resulting source displacement spectra.

We preprocessed the data in the same manner as Eulenfeld *et al.* (2023), differing only in the choice of average shear-wave velocity (3200 m/s), and the selection of log-spaced frequency bands: 13 with central frequencies between 0.75z and 48 Hz (maximum frequency included 50 Hz). For each frequency band, spectral energy density envelopes are calculated using the three seismogram components. The narrowband envelopes are smoothed by convolution with a flat 1-s-long window. The observed envelopes are cut out in a time window starting 1 s before the (provided) *S*-wave onset and ending at an SNR of 2 (but no later than 50 s after *S*-wave onset) and inverted for scattering strength, intrinsic attenuation, and source, and site terms.

We first invert only for the attenuation parameters, using only stations for which the envelope SNR eight seconds after the *S*-wave onset is greater than two, and for events for which this condition is fulfilled on at least five stations. Site and source terms are discarded. In a second step, the attenuation parameters are fixed and the inversion is performed again to constrain the site terms, assuming an average unity site amplification at stations CI.MPM, CI.WBM, and CI.WMF, which have a generally flat frequency response, for all frequency bands. In this and the following step, data from individual stations are included if the SNR five seconds after the *S*-wave onset is greater than two, using events only if this condition is met at three or more stations. In the third iteration, we fix the attenuation parameters and site amplifications and invert for the source terms. Finally, we merge the results from all frequency bands and convert the source terms to a displacement spectrum for each event. The source model is fit to the observed spectra to obtain the seismic moment, corner frequency, and high-frequency fall-off n for each earthquake, with n fixed at its median fitted value of 2.58 in the final step, and we estimate spectral $\Delta\sigma$ following Madariaga (1976). Configuration details, results in JSON format, plots, and the exact invocation of the Qopen commands are made available at Eulenfeld (2024). Study results name: Eulenfeld_Qopen_S.

PBRT (Parker, Baltay, Rekoske, and Thompson): Arias intensity

Parker *et al.* (2020) estimated spectral $\Delta\sigma$ directly from the Arias intensity dataset of Rekoske *et al.* (2019, 2020) following

the method of Baltay *et al.* (2019), which related spectral $\Delta\sigma$ through rms acceleration to Arias intensity. These results only estimate spectral $\Delta\sigma$, so corner frequency was determined assuming moment from the catalog magnitude, from Hanks and Kanamori (1979). Study results name: PBRT_Arias_PS.

Kemna and Harrington: Attenuation model, spectral ratios, and stopping phases

We apply three distinct methods: The first fits individual spectra for exponential attenuation, a Brune source model, and a site effect; the second is a spectral ratio approach; and the third is inversion of stopping phases. All use the same preprocessing which starts with a two-step window-length selection. The first step is magnitude based and selects a window that is sufficiently long to observe a low spectral $\Delta\sigma$-value (0.1 MPa) based on the inverse of the theoretical corner frequency for a given magnitude multiplied by a factor of five. The window is refined in the second step to correspond to a decreasing percentage of the total energy for increasing source-station distances (e.g., 90% for stations < 25 km, 80% for stations between 25–50 km, and 70% at greater distances). We also impose a minimum and maximum duration of 1 and 30 s, for *P* waves, and 1 and 100 s for *S* waves, respectively. The details of the event selection, windowing, spectral fitting, and spectral $\Delta\sigma$ estimation for the first two methods can be found in Kemna *et al.* (2021). Study results names: KemnaHarrington_Qfit_S and KemnaHarrington_SpecRatio_S.

For the inversion of stopping phases, we use acceleration records band-passed between 5 and 20 Hz and cross-correlate each trace with the Hilbert transform to obtain the stopping-phase arrival-time difference Δt (of both *P* and *S* phases, when possible). For cross-correlation coefficients greater than 0.8, we invert for rupture dimension using the Δt and the strike, dip, and rake inferred from focal mechanism solutions for the respective events. The inversion recovers an independent estimate of rupture velocity, for which directivity can be measured given sufficient azimuthal coverage. Study results name: KemnaHarrington_Stopping_S.

Ji and Archuleta: Attenuation modeling

Ji *et al.* (2024) and Mayeda *et al.* (2024) use *S*-wave acceleration records at $\Delta < 50$ km and calculate *Q* models, to constrain the apparent stress and spectral $\Delta\sigma$ for selected moderate earthquakes during the 2019 Ridgecrest sequence. Study results name: JiArchuleta_kappaE_S.

Calderoni: Attenuation modeling and spectral ratio

Calderoni and Abercrombie (2024) describe the application of independent spectral fitting with exponential attenuation and spectral ratios approaches to the Ridgecrest earthquakes, following the methods of Calderoni *et al.* (2019) and Calderoni and Abercrombie (2023). Study results names: Calderoni_kappa_S, Calderoni_SpecRatio_S.

Mayeda: Coda Calibration Tool

Mayeda *et al.* (2024, this issue) apply the Coda Calibration Tool (CCT) empirical coda method (Barno, 2017), based on the approach developed by Mayeda *et al.* (2003) that takes advantage of the stability and azimuthal averaging of coda waves. Study results name: Mayeda_CCT_coda.

Atkinson: Ground-motion model

Atkinson (2024) applies an approach that focuses on the relationship between source spectra and observed ground motion, which is important for the development of ground-motion models used in seismic hazard analysis. She uses the Fourier amplitude spectra data of Rekoske *et al.* (2020) to empirically determine coefficients for source, path, and site functions and ultimately recover source spectra. Study results: Atkinson_GMM.

Boyd: Spectral ratios

We implement a spectral ratio method as detailed in Boyd *et al.* (2017). A maximum hypocentral separation distance of 5 km is used to select the M 3+ earthquakes considered for the analysis (decreased from the 10 km epicentral distance used by Boyd *et al.*, 2017). A total of 51 earthquake sets comprising 600 earthquakes are considered, with the median number of earthquakes in a set being 45, and 95% of the sets having more than 10 events. The median number of spectral ratios contributing to estimates of moment ratio and corner frequencies for an event set are 71 and 116, and 95% of the event sets use more than 5000 spectral ratios. Here, we also modify the windowing of time series prior to calculating signal spectra. Rather than apply a constant window length, one minute before to three minutes after the expected *S*-wave arrival as was done in Boyd *et al.* (2017), which may dilute the frequency content of smaller magnitude earthquakes and/or stations at smaller epicentral distance, significant duration is used (Kempton and Stewart, 2006). This window is a function of earthquake magnitude and distance and can be a factor of 10 or more shorter than the four-minute window used in Boyd *et al.* (2017). A quarter of the significant duration is added before the *S*-wave arrival and to the end of the window prior to application of a 25% cosine taper. On average, this modification to the windowing results in higher corner frequencies (2% larger), higher relative moments for earthquakes smaller than the largest in a set (11% larger), and higher spectral $\Delta\sigma$ (by 18%). The log-standard deviation of spectral $\Delta\sigma$, however, is reduced by 25%. Study results name: Boyd_SpecRatio_coda.

Huang: Spectral ratios

We use *P*-wave spectral ratios between target earthquakes and their EGFs to estimate corner frequencies, following the methods described by Huang *et al.* (2016, 2017) and Liu *et al.* (2020); refer to Abercrombie *et al.* (2025). The EGFs must be at least one magnitude smaller than target events and within about three source dimensions of the target events. This results in 1–5

EGFs for M 2.5–3 earthquakes and 3–7 EGFs for M 3–4.1 earthquakes. We also apply five windows overlapped by half of the window duration to stabilize the spectral ratios and choose the window length that gives the smallest misfits between the Boatwright (1980) spectral model and the stacked spectral ratios. The total window lengths range between 0.9 and 2.4 s for M 2.5–3 earthquakes, and lie within 1.8 and 4.2 s for M 3–4.1 earthquakes. Study results name: Huang_SpecRatio_P.

Abercrombie: Spectral ratios

Abercrombie *et al.* (2025) follows the EGF spectral ratio approach developed by Abercrombie (2014), Abercrombie *et al.* (2017), and Pennington *et al.* (2021). Study results: Abercrombie_SpecRatio P and Abercrombie_SpecRatio_S.

Dreger and Taira: EGF and finite fault

We follow the approach of Dreger (1997) and Dreger *et al.* (2021) using EGF events to isolate the source and attempt finite-fault modeling of the largest events in the study. For each target event, we try EGF events within 1 km hypocentral distance and 1–2.5 M units smaller than the target, and select those with the highest cross correlation. The seismogram time windows start 5 s before the *P*-wave arrival, and we perform complex spectral deconvolution to obtain seismic moment rate functions, stacking the results for the three components at each station. We then invert for kinematic finite-source models following Mori and Hartzell (1990) and Dreger (1997). The two possible nodal planes from either a first-motion mechanism or moment tensor are evaluated to find the best-fitting orientation, and a grid search is used over the rise time and rupture velocity parameters. We follow the approach of Ripperger and Mai (2004) to calculate the average stress drop and peak stress drop from the best-fitting kinematic model. The average is based on the average over subfaults with slip, and which experienced a negative stress change or stress drop (near edges of faults there can be positive stress change). Study results name: DregerTaira_FF_PS.

RESULTS AND DISCUSSION

Here, we present a general overview of the combined results of the Community Validation Study to date. A more detailed analysis of the dataset as a whole is presented by Baltay and Abercrombie (2025) and Abercrombie and Baltay (2025), and of different subsets by many other articles in the issue. At this point in the community study, there is no clear preferred or perfect method, and ongoing work (refer to multiple articles in this issue) is attempting to identify the principal sources of uncertainty. One should consider carefully the effects of simplifying assumptions and the data limitations in a particular study, and to interpret results with care.

Initial submitted results

We first consider spectral $\Delta\sigma$s as submitted from all 56 sets of results (Fig. 3). Note that we use the same legend throughout the article, consistent with the symbols in Figure 2. Enormous scatter in spectral $\Delta\sigma$, over seven orders of magnitude for earthquakes of M 1–7.1, is evident for the dataset as a whole and even for individual, well-recorded events. We also note that many submissions include some extremely high and low values, demonstrating that most of the inversion results require some careful and thoughtful QC before interpretation, as is typically done. Such practices can lead to selection bias (for example, as argued by Shearer and Abercrombie, 2021), and so we prefer to start with the full results included here.

QC and minimizing selection bias

Our first step in analyzing the combined datasets is to perform some initial QC to remove estimates that are the least well resolved, or most likely to be subject to systematic bias. For each set of submitted results, we calculate the moment magnitudes from the submitted moment estimates, using Hanks and Kanamori (1979), and compare these with the M_w-values in the SCSN catalog, obtained from regional moment tensor modeling (Clinton *et al.*, 2006, Fig. 4, Fig. S1). As noted by Trugman (2020) and Shearer *et al.* (2022) many spectral decomposition studies systematically underestimate the moment of larger events because the short time windows needed for the smaller earthquakes fail to sample the long-period level below the corner frequency of the larger events. For each of the spectral decomposition studies, we select a maximum magnitude to include based on the frequency range of the measurements and the relationship between estimated moment and SCSN M_w (refer to Fig. 4, Fig. S1), and previous analysis (Shearer *et al.*, 2022). We consider the difference between the SCSN M_w and the M_w calculated from the submitted M_0 following Hanks and Kanamori (1979). We remove from our analysis all submitted results (corner frequency, spectral $\Delta\sigma$, and moment) for events in the respective datasets that have a catalog preferred magnitude greater than this approximate measurement limit (noted in Fig. 2); we retain all submitted results in the supplemental material.

Recalculating spectral stress drop to be uniform

The submitted spectral $\Delta\sigma$-values (Fig. 3) include many sources of variation related to different choices of assumed parameters to calculate a spectral $\Delta\sigma$ from the spectral measurements of corner frequency and seismic moment. To investigate the real variability we must go back to these estimated model parameters, and so we consider the submitted corner-frequency values as a function of preferred SCSN catalog magnitude, M (Fig. 5a).

To eliminate variability from different spectral $\Delta\sigma$ models, which is not the focus of our study, we select a constant spectral source model to estimate spectral $\Delta\sigma$ from seismic moment and corner frequency using equation (3). We (arbitrarily) choose to use the Madariaga (1976) source model, in which the constant k = 0.32 for *P* waves and

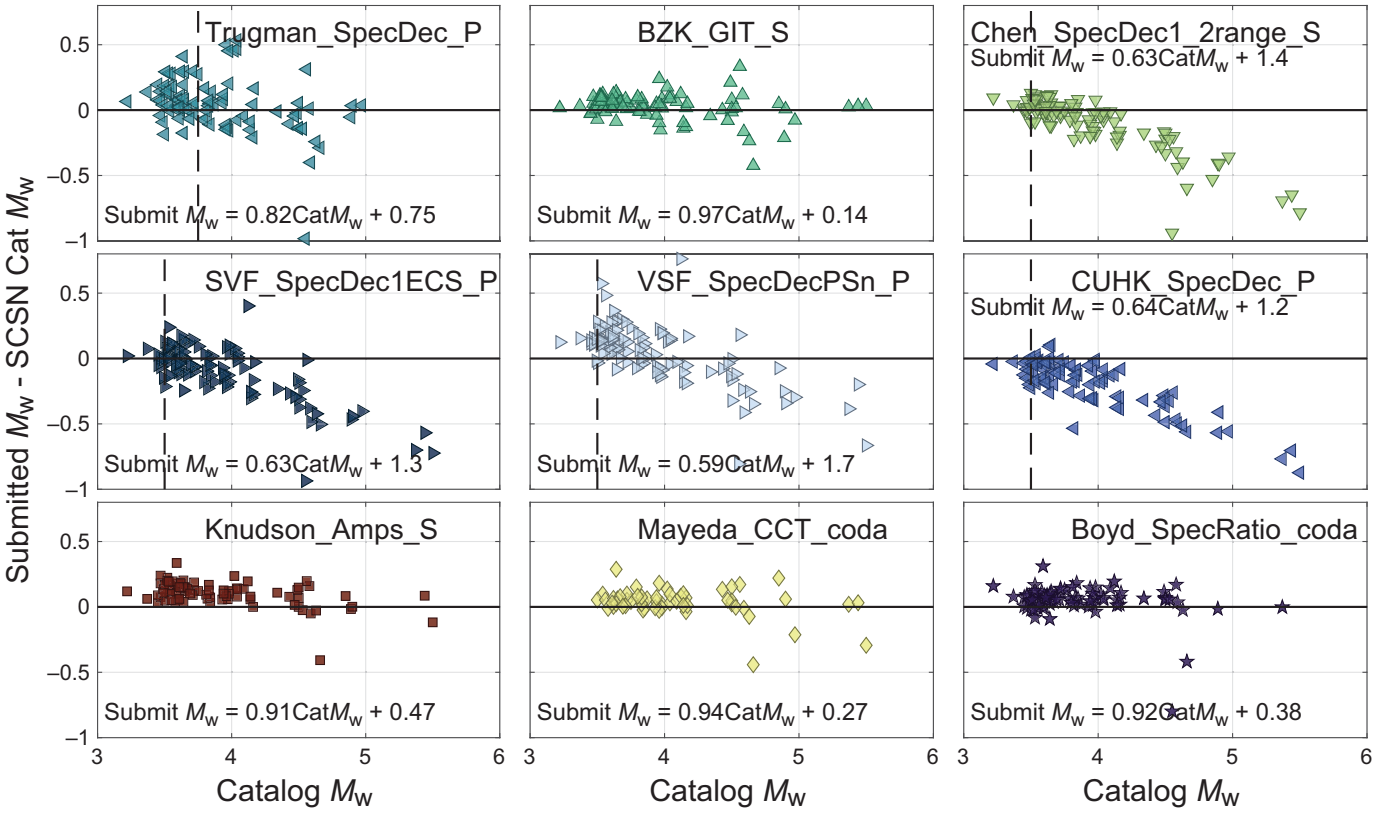

Figure 4. Comparison of the submitted M_w (calculated directly from submitted M_0) to the available SCSN catalog M_w-values for a selected set of results. All results are shown in corresponding Figure S1. Each panel shows results from an individual study, with the linear relationship between the submitted and catalog M_w. The vertical dashed line in some spectral decomposition plots indicates the maximum magnitude of calculated source parameters we use in this analysis; where no vertical dashed line exists, all magnitudes were kept.

0.21 for *S* waves, with a depth-independent shear-wave velocity $\beta = 3500$ m/s and $c = (7/16)$ to represent a circular rupture. Selection of other source models could vary the absolute estimates of spectral $\Delta\sigma$ by over a factor of 5 (e.g., Brune, 1970; Abercrombie and Rice, 2005), but would have no effect on the relative values for particular wave types. The ratio between *P*- and *S*-wave measurements using the same approach can help inform the choice of model and constants as clearly both should yield the same answer (e.g., Abercrombie, 1995; Abercrombie *et al.*, 2017).

Because spectral $\Delta\sigma$ is the ratio of seismic moment to corner frequency cubed, we need consistent seismic moments. We adopt the study seismic moment, which includes submitted seismic moments when available, and otherwise the study catalog moment magnitudes converted to moment, following the relationships of Baltay and Abercrombie (2025), as described in the Data section. With these moments, we estimate spectral $\Delta\sigma$ from the submitted corner frequencies to get the study recalculated stress drop ($\Delta\sigma$) for each event in each submission. These are shown in Figure 5c, and comparison with Figure 3 shows that consistent choice of source model and related parameters decreases the variability in estimated spectral $\Delta\sigma$ by almost an order of magnitude. Variability of estimates for an individual earthquake remains over an order of magnitude, and often nearer two, however, which is still too large. The most likely sources of this variability are uncertainty in isolating the source spectra from the propagation and site effects, as investigated by Shearer *et al.* (2024), and also different approaches to fitting the simple omega source model to real data from earthquake sources (refer to Cochran *et al.*, 2024).

To visualize the difference between different analysis approaches to isolate the source spectra, we separate the results by method (Fig. 6) revealing the large systematic differences between the different studies and indicating that much of the interstudy variation results from nonrandom, but systematic variation.

Relationship between *P*- and *S*-wave corner frequencies

There were submissions from five studies that contained both *P*- and *S*-wave measurements using the same methods, allowing a comparison of the ratio of the calculated f_{cP} to f_{cS}; four are spectral decomposition and one is spectral ratios (Fig. 7). All show correlations, which are higher when the smallest events are excluded. The correlations between submitted spectral $\Delta\sigma$-values (0.1–0.8) are systematically lower than those between submitted corner-frequency values (0.6–0.8)

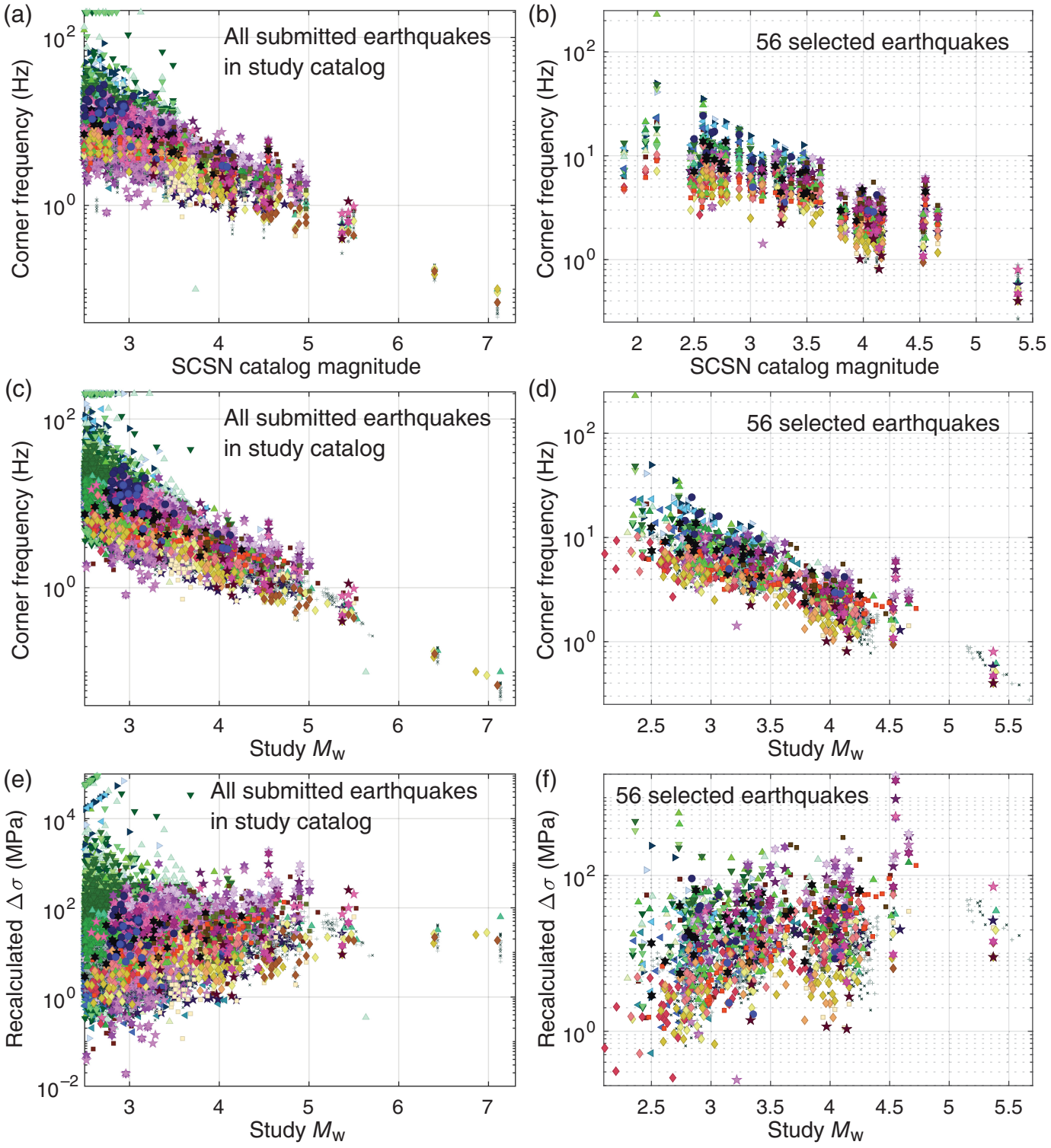

Figure 5. Submitted corner frequency compared to both (a,b) SCSN catalog preferred magnitude (which is mixed M_w, M_L, and M_{Lr}) and (c,d) study M_w (which uses submitted M_0 combined with M_wBA). (e,f) Consistently recalculated study Madariaga (1976) stress drop from submitted corner frequency and study moment (using same constants and source model) versus study moment magnitude. (a,c,e) All earthquakes; (b,d,f) just the 56 events. Please refer to Figures 2 and 3 for legend.

because the corner-frequency estimates include an underlying correlation with magnitude. This difference is good to remember when comparing results from different studies and using the agreement to support resolution of source parameter results.

Different source models predict different ratios of the corner frequencies of the *P* and *S* waves (e.g., Madariaga, 1976; Kaneko and Shearer, 2015), and so agreement between calculated

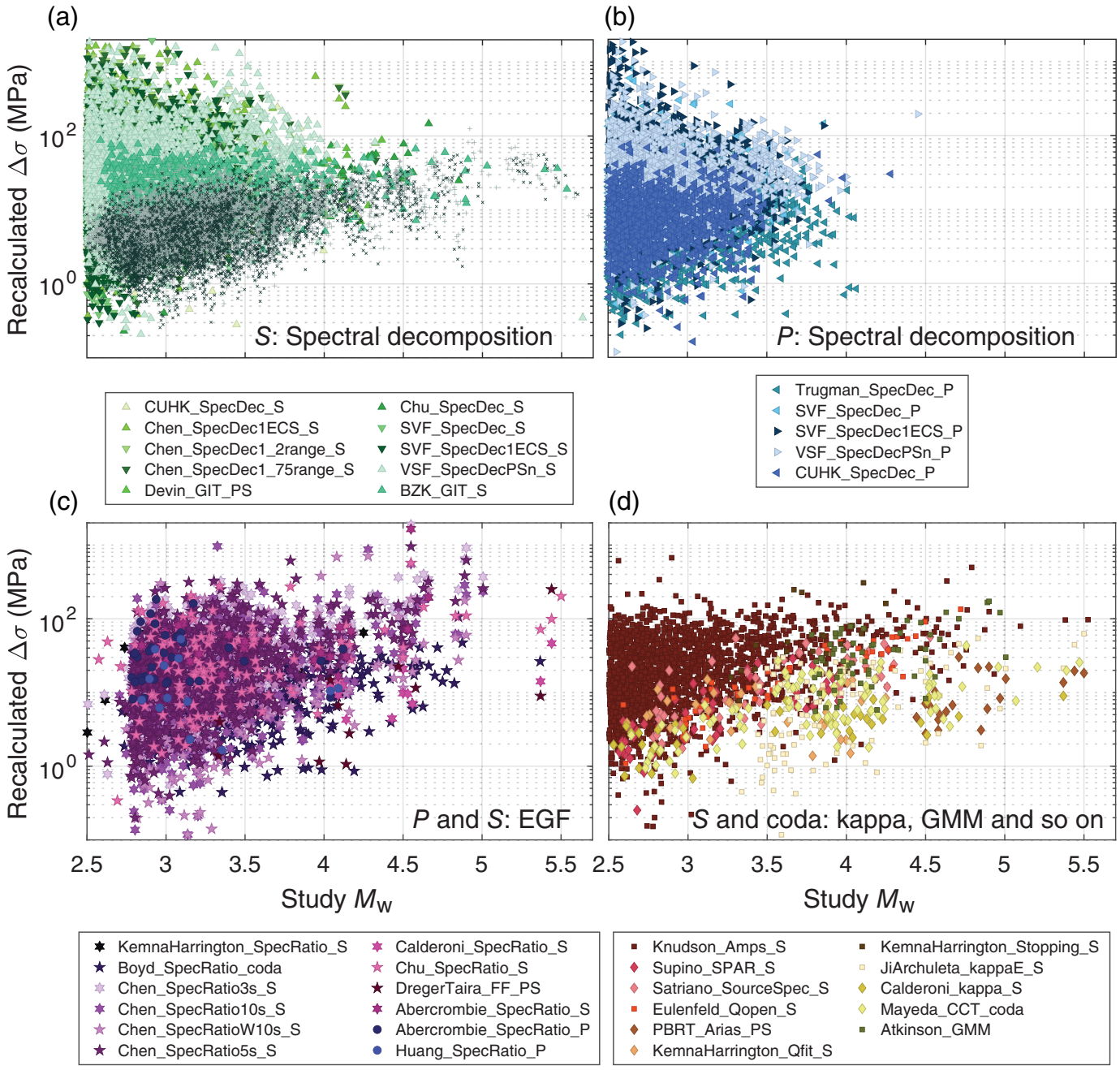

Figure 6. Consistently recalculated study spectral $\Delta\sigma$ from submitted corner frequency and study moment, by method type: (a) the greens indicate *S*-wave spectral decomposition and generalized inversion technique (GIT), (b) the blues indicate *P*-wave spectral decomposition and GIT, (c) the pinks and purples: *P*- and *S*-wave empirical Green's function (EGF) spectral ratio, and (d) the oranges and browns: *S*- and coda wave with other approaches, including attenuation models.

estimates of stress drop will depend on whether the ratio of the estimated *P*- and *S*-wave corner frequencies matches that of the model selected. Many studies use the ratio of $f_{cP}/f_{cS} = 1.5$ from Madariaga (1976) or the ratio of *P*-wave velocity to *S*-wave velocity at the source, following Hanks and Wyss (1972) but some use others based on the f_c observations (Fig. 2). The question of the corner-frequency shift has been around for decades (e.g., Hanks, 1981; Abercrombie, 1995), and is fundamental to determining correct models of source finiteness and radiated energy. The true ratio of corner frequencies, or pulse durations, remains unresolved because it depends on the correct isolation of source radiation, and hence correct resolution of the trade-offs between path and source that underlie many contributions to this issue.

Formal error bars and intermethod variation

Some of the studies also submit calculated uncertainties on their corner-frequency estimates, and we show these for the subset of eight selected events selected for a detailed comparison (Table 1) in Figure 8. The different studies used different approaches to

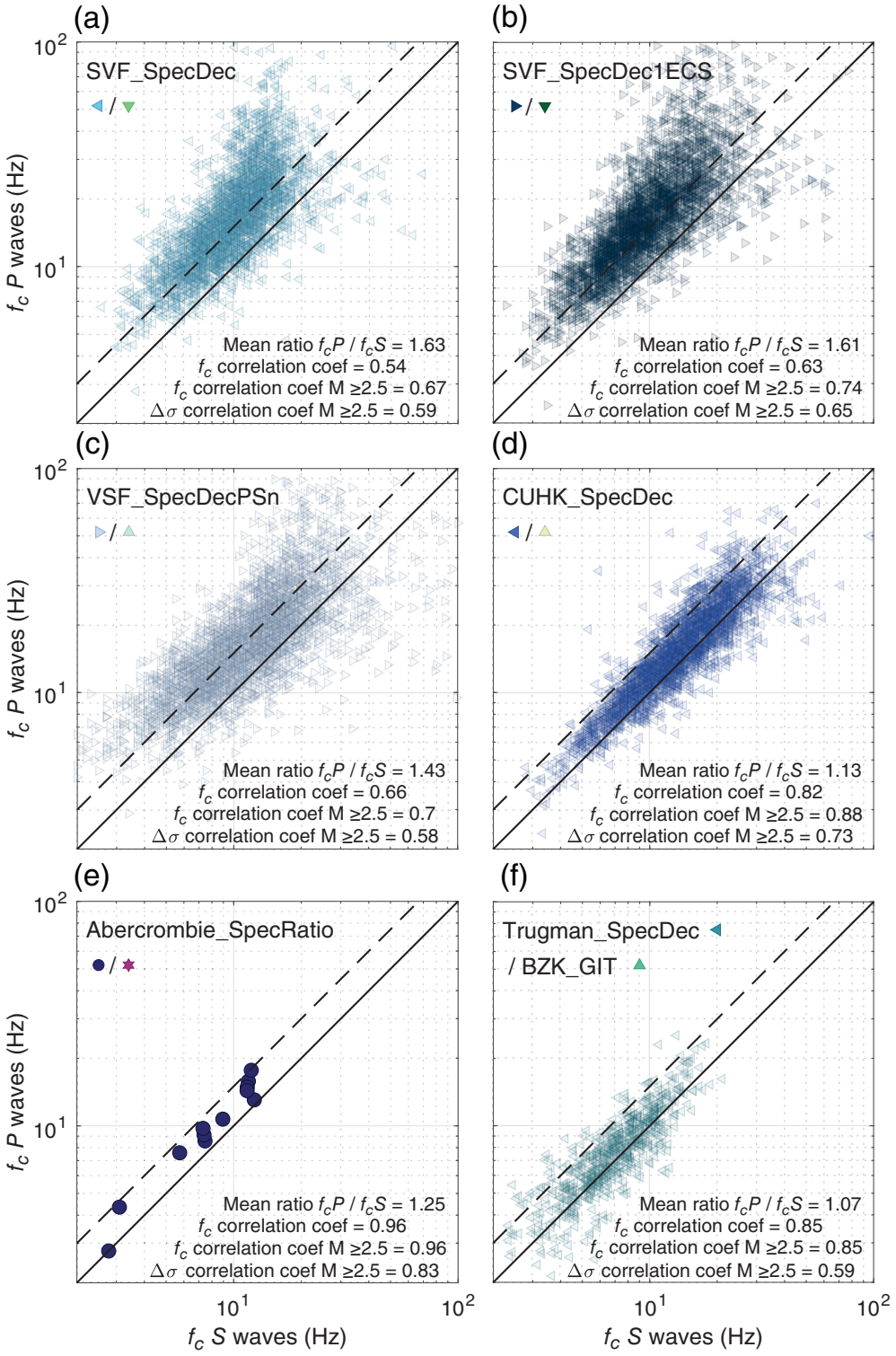

Figure 7. Relationship between (a–f) *P*- and *S*-wave corner frequencies for the five studies (four spectral decomposition, one spectral ratio) that submitted both, and the relationship of the previously published inversion studies (Trugman, 2020, *P* waves and Bindi *et al.*, 2021, *S* waves). The solid lines are 1:1; the dashed lines are 1.5:1 (Madariaga, 1976, model *P/S* relation). The mean ratio is between all values (<50 Hz) submitted, the f_c correlation coefficient is between the same values, and the other coefficients are for the submitted values for M ≥ 2.5 only.

calculate and report uncertainties, and so we converted them to ∼95% confidence limits (or 1.96 × standard deviation or error) to obtain something roughly comparable and indicative. None of the error bars are large enough to encompass the range of values obtained by the different approaches. As noted in the previous work (e.g., Huang *et al.*, 2017; Abercrombie, 2021), the formal statistical uncertainties calculated in individual models are typically smaller than the actual variation between different methods. The formal uncertainties substantially underestimate the real uncertainties because they typically do not include uncertainty in model selection, isolation of source spectra, and choice of assumed constants. Ideally, we would like consistent measurements from all the studies lying within calculated uncertainties, but if the large variation is a result of the data quality and real uncertainties, then we need to find a better way of calculating and presenting the real uncertainties in measurements. Even if we cannot agree on the "best" values for source parameters, then we at least need to ensure that the error bars of published results overlap.

A duplication in the SCSN catalog from the height of the aftershock sequence, and in the catalog used for the community study provides an opportunity to test for consistency within individual approaches. Events 38578455 and 38578439 have origin times within 1 ms of one another, and the magnitudes are within 0.01 unit, suggesting that they are the same event, accidentally given two IDs during the time

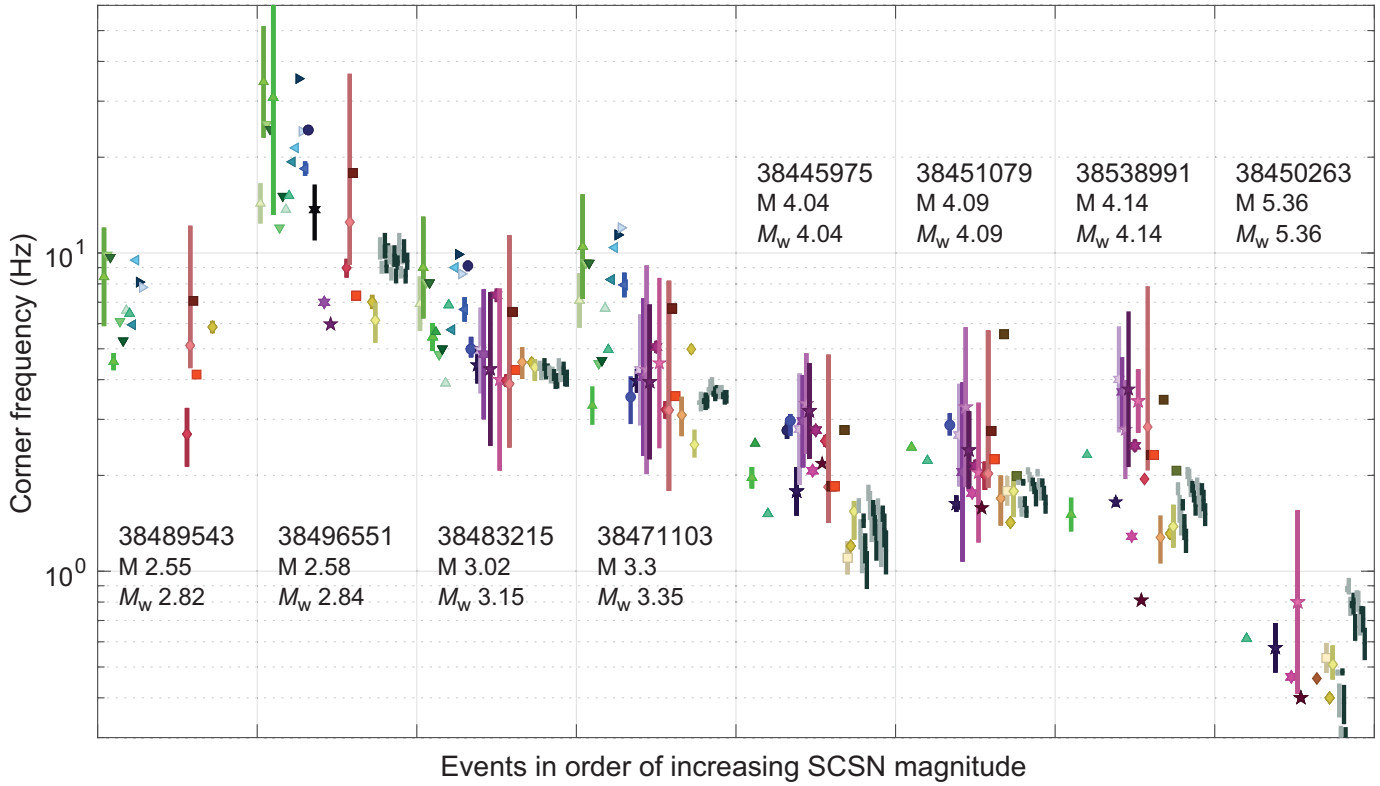

Figure 8. Submitted error bars for eight selected events do not all overlap: Corner-frequency error bars plotted for studies that included them, 95% confidence limits. M is the preferred SCSN catalog magnitude; M_w is the (community) study M_w (as defined in the Data section). Information for individual events is separated by gray vertical lines. Please refer to Figures 2 and 3 for legend.

of high seismicity rate. Event 38578455 has since been deleted from the online SCSN catalog. Fourteen sets of submitted results include estimates for both copies of the duplicate event, providing an opportunity to compare them for consistency (Fig. 9). The moment estimates are closer than those of the corner frequency; the corner-frequency estimates are almost all consistent within 10% or better. This suggests that fitting within a single approach is highly reproducible, but still represents a factor of 30% variation in spectral $\Delta\sigma$, even when the same waveforms are considered, albeit with potentially slightly different starting conditions.

To investigate and visualize the large-scale systematic variations between methods more closely, we calculate average values for the larger sets of results in discrete moment bins (Fig. 10). These figures enable the reader to determine which approaches lead to higher or lower stress-drop estimates. They also reveal how different methods produce different scaling of spectral $\Delta\sigma$, and that all vary across the moment range. Shearer *et al.* (2024) demonstrate how the determination of path and site corrections can explain much of these differences. The lower estimates of spectral $\Delta\sigma$ typically have smaller corrections for attenuation and the inherent frequency dependence of the corrections means that the same estimates tend to have stronger scaling with seismic moment. Different methods use either large, lower-frequency (e.g., Calderoni and Abercrombie, 2024; Mayeda *et al.*, 2024, both this issue) or small, higher-frequency earthquakes (e.g., Shearer *et al.*, 2022; Vandevert *et al.*, 2024) to make the corrections, which suggests they may be more reliable in different moment ranges.

Can we resolve any real variability between earthquakes?

Finally, we consider systematic offsets between methods to determine if the relative variation is consistent. Previous analyses (e.g., Shearer *et al.* 2019; Abercrombie, 2021; Pennington *et al.*, 2021) have found that the relative variability within a method is substantially more reliable than the absolute values. Abercrombie *et al.* (2017) also found that the small-scale variability of earthquake source parameters within one small sequence is much larger than the variation in average values between earthquake sequences in distinctly different tectonic regions. Despite the large variation in estimates between methods, and the corresponding large uncertainties in absolute spectral $\Delta\sigma$ estimates, can we resolve reliable differences between earthquakes within the sequence, and possible spatial and temporal variations? Is there any interesting "signal" within the "noise"?

Using our recalculated study spectral $\Delta\sigma$s based on the Madariaga (1976) model, we examine all 56 events across the full spectrum of methodologies, assessing both the dispersion and the mean trend (Fig. 11). For the selected 56 events, over all 56 methods, all events were studied by at least 15 methods, some events were studied by as many as 48 methods, and the average event was analyzed by 37 methods.

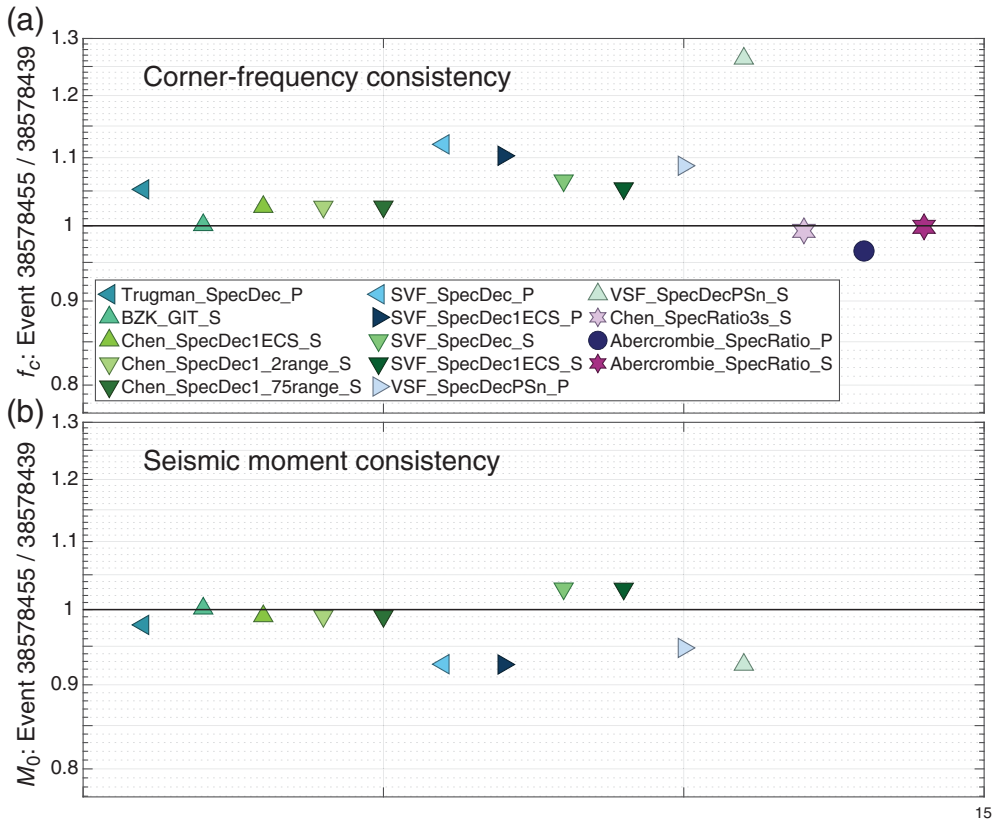

Figure 9. (a,b) Comparison of submitted results for a duplicate event. The high level of consistency suggests that most methods are highly reproducible and not affected by small input differences.

Individually, the majority of methods (47) analyzed at least 26 events, with some considering as many as 55 events, but some methods only considered a few events (as few as 2).

We first average over all the methods that considered each event using a weighted average to account for multiple iterations of similar methods. Specifically, authors that submitted multiple results using variations on a theme (either *P* versus *S* waves, different window lengths, different source models, etc.) were down-weighted such that that author-method received a total weight of 1. For example, Bindi *et al.* (2023a,b) submitted 18 variations on a theme of spectral decomposition with varying *S*-wave window durations, attenuation models, methods for site constraint, and two different source models. Therefore, each of these methods was down-weighted to be 1/18 as compared to an author submission that only had 1 iteration. With the weighting scheme, we obtain a single corner frequency per event (Fig. 11, open-cross circles) then use the selected 56 events to determine an overall magnitude-independent averaged Madariaga (1976) spectral $\Delta\sigma$ of 15.4 MPa (dashed line in Fig. 11a).

We next consider the residual corner frequency, from the average spectral $\Delta\sigma$ of 15.4 MPa, so that the f_c residual is simply the $\log_{10} f_c$ minus the dashed line of constant spectral $\Delta\sigma$ (Fig. 11b). The variability of the corner-frequency submissions is considered in two ways: the first is the variability within each event (between methods that analyzed that event) which we term the within-event variability (similarly to ground-motion modeling methodology, i.e., Baltay *et al.*, 2017); the second is the overall distribution of the average f_c or spectral $\Delta\sigma$ of the collection of 56 events, which we term the between-event variability. We define the first, the within-event variability, as the standard deviation of $\log_{10} f_c$, given for each of the 56 events below each event (Fig. 11b). These values range from 0.08 to 0.36, $\log_{10}$ units. Events with lower within-event standard deviation have more agreement between methods, and we can be more certain of the event corner frequency; these events may be simpler or more "Brune-like", such that they are easier to model (e.g., Cochran *et al.*, 2024). Events with larger standard deviation have much more disagreement between methods. Perhaps those events are more complex or methods struggle to isolate the source component from the attenuation.

The between-event variability of the overall distribution of the 56 events is characterized as the $\text{std}(\log_{10} f_c) = 0.30$ with one f_c per event (i.e., the standard deviation of the open-cross circles in Fig. 11b); we also consider the variability of the recalculated spectral $\Delta\sigma$, using a consistent study catalog moment for each event: $\text{std}(\log_{10} \Delta\sigma) = 0.36$, again with one average spectral $\Delta\sigma$ per event. We can also consider the same metric $\text{std}(\log_{10} \Delta\sigma)$ but for each method individually: for the 52 methods that estimate stress drop for at least 10 of the 56 events, the $\text{std}(\log_{10} \Delta\sigma)$ range from 0.27 to 0.75 with an average of 0.43. This implies that simply harnessing multiple methods averaged together can reduce the variability compared to individual methods.

High-frequency ground motion, such as PGA is dependent on, and thus correlated with spectral $\Delta\sigma$ (e.g., Hanks, 1979; Lior and Ziv, 2017). The potential to use spectral $\Delta\sigma$ as a predictor in ground-motion modeling is compelling yet challenging given: (1) the variability (as demonstrated in this Community Study) of spectral $\Delta\sigma$ compared to the variability evident in PGA; and (2) the difficulty in predicting spectral $\Delta\sigma$ for future events. Cotton *et al.* (2012) discussed the inconsistency in the variability of spectral $\Delta\sigma$ in comparison to the

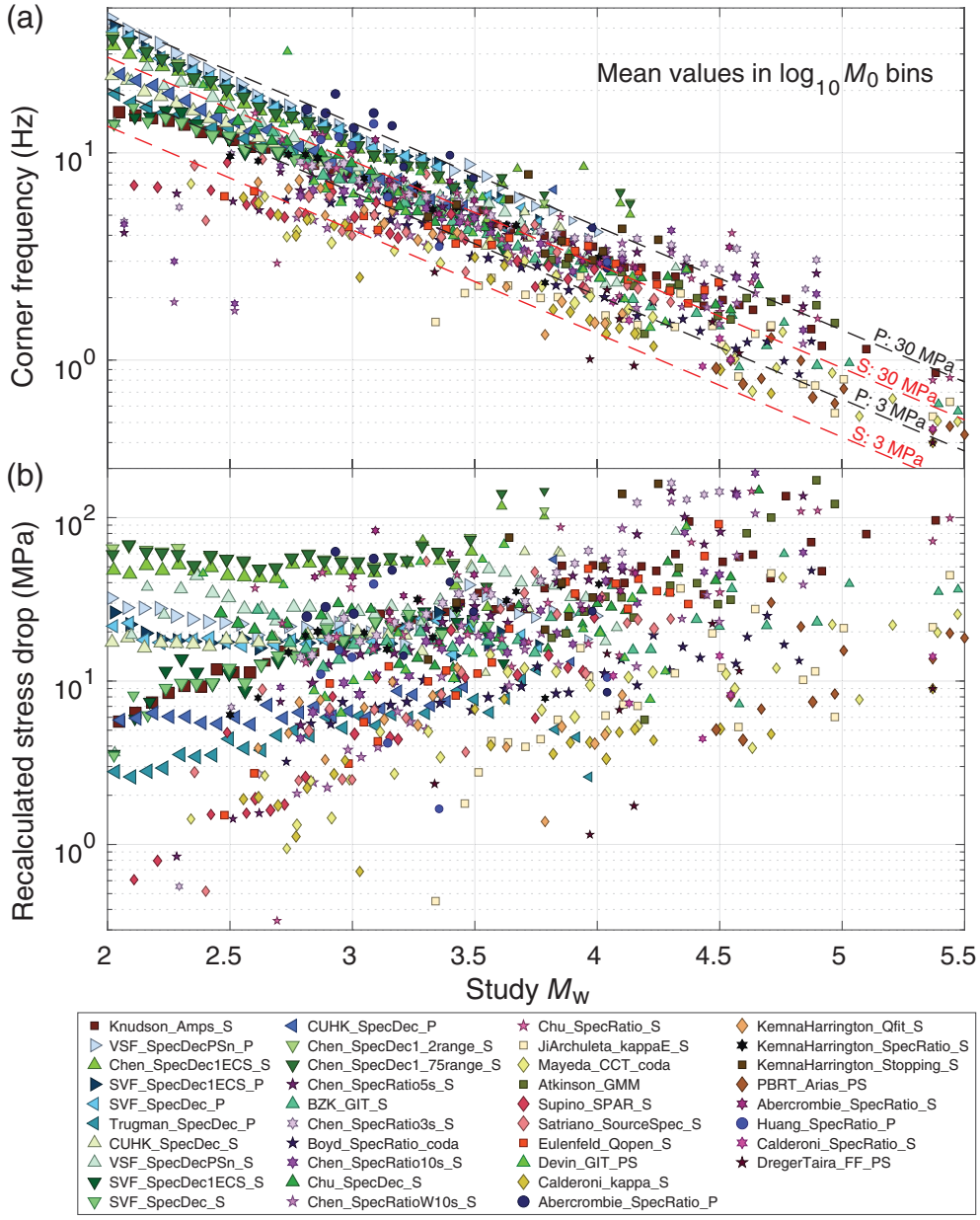

Figure 10. (a) Corner frequency and (b) study recalculated spectral $\Delta\sigma$ averaged in discrete moment bins to show systematic offsets and trends in larger studies. The dashed lines in panel (a) show constant stress drop trends for *P* and *S* waves.

between-event variability in ground-motion models. Other spectral $\Delta\sigma$ studies have typically found variability to be in the range of 0.25–0.75 $\log_{10}$ units (Baltay and Hanks, 2015; Baltay *et al.*, 2019), whereas the standard deviation of PGA, after taking a factor of 0.8 into account to convert from spectral $\Delta\sigma$ to PGA of PGA $\sim \Delta\sigma^{0.80}$ (Boore, 1983), is on the order of 0.11–0.28 $\log_{10}$ units (Cotton *et al.*, 2012, accounting for a factor of 2.3 between ln and $\log_{10}$). Our std($\Delta\sigma$) = 0.36 averaged over all methods is similar to the upper limit of variability of PGA, implying that we reduce the overall variability by harnessing multiple methods to get a more robust result of spectral $\Delta\sigma$, and thus presenting a potential path forward for incorporating spectral $\Delta\sigma$ into ground-motion modeling efforts. Some ground-motion models (e.g., Yenier and Atkinson, 2015) include spectral $\Delta\sigma$ directly as an adjustable model parameter, so fully quantifying its distribution is key for ground-motion modeling efforts.

When investigating the corner-frequency residuals themselves (Fig. 11b), we can start to see both real variations in events (i.e., some events are clearly below the average and some are entirely above the average), as well as consistency in methods that are systematically high or low. Also for several events, all observations agree that a particular event has either a high or low spectral $\Delta\sigma$, with all estimates being above or below the zero line. The statistical separation of certain events implies that some underlying physics is controlling the differences in spectral $\Delta\sigma$ between these events and offers optimism for unraveling these complexities.

CONCLUSIONS

The SCEC/USGS Community Stress Drop Validation Study demonstrates the power of collaboration and communication in tackling the real causes underlying a major source of controversy in earthquake science. That the global community has come together to openly share results is a testament to the interest in this controversial topic. The large compilation of independently obtained results distributed herein provides an unprecedented opportunity to explore features, trends, and differences in spectrally obtained earthquake parameters. The compiled dataset (Baltay *et al.*, 2024) and results also provide a useful benchmark for assessing the quality of new approaches. At this point in time, there is no clear preferred method, and the user must carefully consider the effects of any inherent assumptions and data

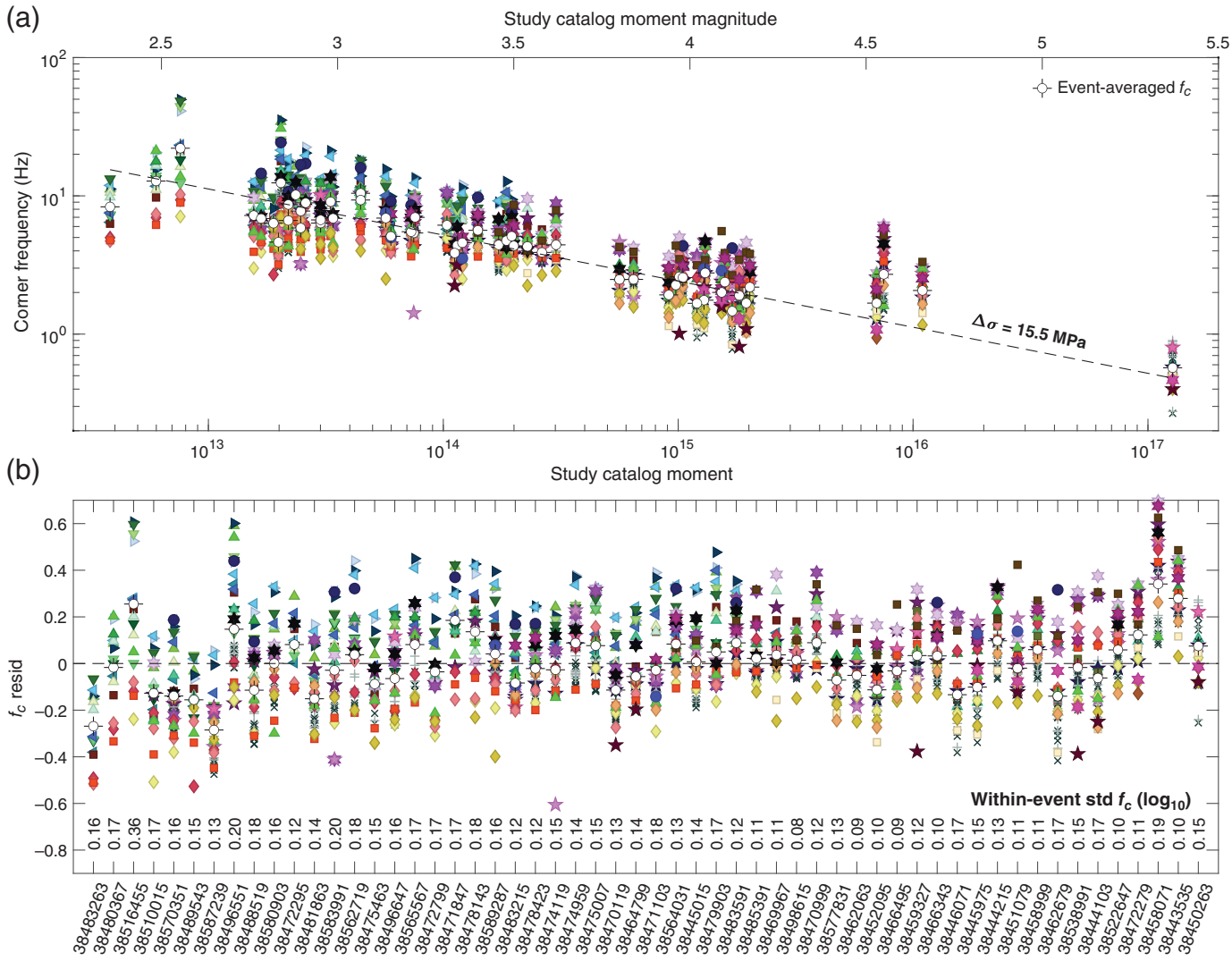

limitations when attempting to interpret results. Baltay and Abercrombie (2025) and Abercrombie and Baltay (2025) provide a more in depth first analysis and comparison of the current approaches.

1. The observed scatter in spectral stress-drop (spectral $\Delta\sigma$) estimates has a large systematic component. There are orders-of-magnitude variation in median spectral $\Delta\sigma$-values among different methods, with the largest variations seen in the smaller magnitude events. Most of this variation likely comes from differences in correcting seismograms and spectra for near-source and site effects, and along-path propagation effects, but given the sheer numbers of small events, we are also more likely to observe extreme values at the smaller magnitudes.
2. Removing the measurements clearly outside the frequency ranges of the available data reduces both between-event and between-method scatter. We recommend users carefully consider the impact of limited bandwidth on results and remove potentially biased values, as we have done here, to prevent subsequent misinterpretation.

Figure 11. (a) Corner frequency for all submissions with weighted event-averaged values in open cross circles and constant spectral $\Delta\sigma$ line of 15.4 MPa. (b) Corner-frequency residual to the constant spectral $\Delta\sigma$ line, spaced out per event for visual clarity, in increasing magnitude order, with within-event standard deviation given below each event. Refer to Figures 2 and 3 for the legend.

3. Use of a consistent source model to obtain spectral $\Delta\sigma$ from the spectral measurements, with the same constants, assumed velocity, and so forth, removes nearly an order of magnitude of systematic scatter.
4. Comparison of studies that use both *P*- and *S*-wave results (five studies here) are too varied to place strong constraints on the real corner-frequency shift. The correlations between *P*- and *S*-wave corner-frequency estimates are systematically higher than those of the spectral $\Delta\sigma$ estimates derived from them. This demonstrates that much of the apparent correlation between *P*- and *S*-wave corner frequencies results from the underlying magnitude dependence, as all studies find decreasing corner frequency with increasing magnitude for the dataset as a whole.

5. Model-based estimates of uncertainty submitted by participants do not always overlap, even after we account for different source models and assumed constants. This implies that parameter and processing choices are not covering the full range of possible behavior and suggests that most published error estimates substantially underestimate the real (epistemic) uncertainty in the estimated source parameters.
6. The large-scale trends of spectral $\Delta\sigma$, for example with magnitude, are very dependent on the method assumed to isolate and model the source. Relative event-to-event variability, for earthquakes of similar magnitude from an individual study, is more consistent between different methods and more reliable than apparent overall trends. This suggests that real, physically based variations in earthquake sources may be resolvable.

DATA AND RESOURCES

The common waveform database and associated metadata are described by Baltay *et al.* (2024), and are available for download at the Southern California Earthquake Data Center (SCEDC): https://scedc.caltech.edu/data/stressdrop-ridgecrest.html (last accessed October 2021). Along with full waveform data from stations within 1° of the earthquake locations (Fig. 1b), we have provided phase picks and metadata, including the Trugman (2020) catalog with updated SCSN magnitudes (https://service.scedc.caltech.edu/eq-catalogs/date_mag_loc.php; last accessed June 2024). For more details on the waveform data including stations and processing details, please refer to Baltay *et al.* (2024). All the waveform data and metadata references used in the analysis are publicly available (Baltay *et al.*, 2024) and accessible from the SCEDC (SCEDC, 2013; doi: 10.7909/C3WD3xH1), Incorporated Research Institutions for Seismology (IRIS; https://ds.iris.edu/ds/nodes/dmc/, last accessed October 2021) and Northern California Earthquake Data Center (NCEDC; doi: 10.7932/NCEDC). The SCEDC and Southern California Seismic Network (SCSN) are funded through U.S. Geological Survey (USGS) Grant G20AP00037, and the Southern California Earthquake Center, which is funded by National Science Foundation (NSF) Cooperative Agreement EAR-0529922 and USGS Cooperative Agreement 07HQAG0008. IRIS Data Services are funded through the Seismological Facilities for the Advancement of Geoscience and EarthScope (SAGE) Proposal of the NSF under Cooperative Agreement EAR-1261681. Networks that provided data are: CE (California Geological Survey, 1972); CI (California Institute of Technology and U.S. Geological Survey [USGS] Pasadena, 1926); GS (Albuquerque Seismological Laboratory [ASL]/USGS, 1980); NN (University of Nevada, Reno, 1971); NP (USGS, 1931); PB (https://www.fdsn.org/networks/detail/PB/); SN (University of Nevada, Reno, 1992); and ZY, https://www.fdsn.org/networks/detail/ZY_1990/ (Cochran *et al.*, 2020). All data referenced here are available at the SCEDC (SCEDC, 2013) at https://scedc.caltech.edu/data/stressdropridgecrest.html (last accessed October 2021), in which a "Quick-reference guide" is also posted for more information on the waveform data. The SCSN catalog change history is available from https://scedc.caltech.edu/eq-catalogs/change-history.html (last accessed March 2025). The supplemental material contains a Fourier amplitude spectrum (FAS) flatfile, Figures S1 and S2, and Table S1, a zip folder of.csv for each author-submission (56 total) at https://cloud.seismosoc.org/s/ksyAo2L8G8QaDnm (last accessed April 2025). Compiled results for the 56 events including the submitted corner frequency, best moment, and best magnitude for each method.

DECLARATION OF COMPETING INTERESTS

The authors acknowledge that there are no conflicts of interest recorded.

ACKNOWLEDGMENTS

The authors and PIs of this research project are appreciative of all the global community support and enthusiasm for this collaborative work, and thank and acknowledge everyone who has participated in the various workshops and discussions. The authors also thank the editors and reviewers who handled this article, improving its quality, including T. Uchide and B. Enescu. This research was supported by Southern California Earthquake Center (SCEC) (Award Numbers 24067, 23107, 23108, 22034, 22042, 22101, 22027, 21032, 21045, 21083, 21114, and 21169, including salary support for T. Taira, D. Dreger, C. Ruhl, X. Chen, P. Shearer, X. Chen, Q. Wu, W. Ellsworth, T. Knudsen, and financial support for the 2022 September workshop). The authors are also grateful to T. Huynh and E. Pauk for their invaluable logistical support. R. Abercrombie is grateful for U.S. Geological Survey (USGS) support though an IPA for her contribution to the project. SCEC is funded by National Science Foundation (NSF) Cooperative Agreement EAR-1600087 and USGS Cooperative Agreement G17AC00047. SCEC Contribution Number 13471. The work of W. Walter and C. N. Pennington was completed at LLNL under Contract DE-AC52-07NA2734. J. Zhang and H. Yang are supported by Hong Kong Research Grant Council (Awards 14306122 and 14308523).
Any use of trade, firm, or product names is for descriptive purposes only and does not imply endorsement by the U.S. Government.

REFERENCES

Abercrombie, R. E. (1995). Earthquake source scaling relationships from −1 to 5 ML using seismograms recorded at 2.5-km depth, *J. Geophys. Res.* **100,** no. B12, 24015–24036, doi: 10.1029/95JB02397.

Abercrombie, R. E. (2014). Stress drops of repeating earthquakes on the San Andreas Fault at Parkfield, *Geophys. Res. Lett.* **41,** 8784–8791, doi: 10.1002/2014GL062079.

Abercrombie, R. E. (2015). Investigating uncertainties in empirical Green's function analysis of earthquake source parameters, in *J. Geophys. Res.* **120,** 4263–4277, doi: 10.1002/2015JB011984.

Abercrombie, R. E. (2021). Resolution and uncertainties in estimates of earthquake stress drop and energy release, *Phil. Trans. R. Soc. Lond. A* **379,** doi: 10.1098/rsta.2020.0131.

Abercrombie, R. E., and A. S. Baltay (2025). Magnitude, depth and methodological variations of spectral stress drop within the SCEC/USGS community stress drop validation study using the 2019 Ridgecrest earthquake sequence, *Bull. Seismol. Soc. Am.* (submitted).

Abercrombie, R. E., and J. R. Rice (2005). Can observations of earthquake scaling constrain slip weakening?, *Geophys. J. Int.* **162,** no. 2, 406–424, doi: 10.1111/j.1365-246X.2005.02579.x.

Abercrombie, R. E., S. Bannister, J. Ristau, and D. Doser (2017). Variability of earthquake stress drop in a subduction setting, the Hikurangi Margin, New Zealand, *Geophys. J. Int.* **208,** 306–320, doi: 10.1093/gji/ggw393.

Abercrombie, R. E., X. Chen, Y. Huang, and S. Chu (2025). Comparison of EGF methods for Ridgecrest Sequence: Can EGF be used to help resolve ambiguity in isolating source spectra? *Bull. Seismol. Soc. Am.* doi: 10.1785/0120240161.

Afshari, K., and J. P. Stewart (2016). Physically parameterized prediction equations for significant duration in active crustal regions, *Earthq. Spectra* **32,** 2057–2081, doi: 10.1193/063015EQS106M.

Aki, K. (1967). Scaling law of seismic spectrum, *J. Geophys. Res.* **72,** 1217–1231, doi: 10.1029/JZ072i004p01217.

Albuquerque Seismological Laboratory (ASL)/U.S. Geological Survey (USGS) (1980). *U.S. Geological Survey Networks* [Data set], *International Federation of Digital Seismograph Networks*, doi: 10.7914/SN/GS.

Al-Ismail, F., W. L. Ellsworth, and G. C. Beroza (2023). A time-domain approach for accurate spectral source estimation with application to Ridgecrest, California, earthquakes, *Bull. Seismol. Soc. Am.* **113,** no. 3, 1091–1101, doi: 10.1785/0120220228.

Andrews, D. J. (1986). Objective determination of source parameters and similarity of earthquakes of different size, in *Earthquake Source Mechanics*, S. Das, J. Boatwright, and C. H. Scholz (Editors), AGU, Washington, D. C., 259–268.

Atkinson, G. M. (2024). Impact of geometric spreading in the Fourier domain on source spectra: observations of steep amplitude decay and frequency dependence from the 2019 Ridgecrest, California earthquake sequence, *Bull. Seismol. Soc. Am.* doi: 10.1785/0120240005.

Atkinson, G. M., and I. Beresnev (1997). Don't call it stress drop, *Seismol. Res. Lett.* **68,** no. 1, 3–4, doi: 10.1785/gssrl.68.1.3.

Baltay, A., R. Abercrombie, S. Chu, and T. Taira (2024). The SCEC/USGS community stress drop validation study using the 2019 Ridgecrest earthquake sequence, *Seismica* **3,** no. 1, doi: 10.26443/seismica.v3i1.1009.

Baltay, A. S., and R. E. Abercrombie (2025). Seismic moment and local magnitude scales in Ridgecrest, CA from the SCEC/USGS Community Stress Drop Validation Study *Bull. Seismol. Soc. Am.* doi: 10.1785/0120240162.

Baltay, A. S., and T. C. Hanks (2015). Stress drop variability and its relationship to variability in GMPEs, *SSA Annual Meeting 2015*, Seismological Research Letters, Vol. 86, Pasadena, California, 21–23 April 2015.

Baltay, A. S., T. C. Hanks, and N. A. Abrahamson (2017). Uncertainty, variability, and earthquake physics in ground-motion prediction equations, *Bull. Seismol. Soc. Am.* **107,** no. 4, 1754–1772, doi: 10.1785/0120160164.

Baltay, A. S., T. C. Hanks, and N. A. Abrahamson (2019). Earthquake stress drop and Arias intensity, *J. Geophys. Res.* **124,** 3838–3852, doi: 10.1029/2018JB016753.

Barno, J. (2017). LLNL/coda-calibration-tool, *Computer Software*, USDOE, doi: 10.11578/dc.20180306.1.

Bindi, D., H. N. T. Razafindrakoto, M. Picozzi, and A. Oth (2021). Stress drop derived from spectral analysis considering the hypocentral depth in the attenuation model: Application to the Ridgecrest Region, California, *Bull. Seismol. Soc. Am.* **111,** no. 6, 3175–3188, doi: 10.1785/0120210039.

Bindi, D., D. Spallarossa, M. Picozzi, A. Oth, P. Morasca, and K. Mayeda (2023a). The community stress-drop validation study—part I: Source, propagation, and site decomposition of Fourier spectra, *Seismol. Res. Lett.* **94,** no. 4, 1980–1991, doi: 10.1785/0220230019.

Bindi, D., D. Spallarossa, M. Picozzi, A. Oth, P. Morasca, and K. Mayeda (2023b). The community stress-drop validation study—part II: Uncertainties of the source parameters and stress drop analysis, *Seismol. Res. Lett.* **94,** no. 4, 1992–2002, doi: 10.1785/0220230020.

Bindi, D., D. Spallarossa, M. Picozzi, A. Oth, P. Morasca, and K. Mayeda (2023c). Spectral decomposition results for the SCEC-community stress drop validation study, *GFZ Data Services*, doi: 10.5880/GFZ.2.6.2023.005.

Bindi, D., R. Zaccarelli, and S. R. Kotha (2020). Local and moment magnitude analysis in the Ridgecrest Region, California: Impact on interevent ground-motion variability, *Bull. Seismol. Soc. Am.* **111,** no. 1, 339–355, doi: 10.1785/0120200227.

Boatwright, J. (1980). A spectral theory for circular seismic sources; simple estimates of source dimension, dynamic stress drop, and radiated seismic energy, *Bull. Seismol. Soc. Am.* **70,** 1–27.

Boore, D. M. (1983). Stochastic simulation of high-frequency ground motions based on seismological models of the radiated spectra, *Bull. Seismol. Soc. Am.* **73,** 1865–1894.

Boyd, O. S., D. E. McNamara, S. Hartzell, and G. Choy (2017). Influence of lithostatic stress on earthquake stress drops in North America, *Bull. Seismol. Soc. Am.* **107,** no. 2, doi: 10.1785/0120160219.

Brune, J. N. (1970). Tectonic stress and the spectra of seismic shear waves from earthquakes, *J. Geophys. Res.* **75,** 4997–5009, doi: 10.1029/JB075i026p04997.

Brune, J. N. (1971). Correction [to "Tectonic stress and the spectra of seismic shear waves from earthquakes"], *J. Geophys. Res.* **76,** 5002, doi: 10.1029/JB076i020p05002.

Calderoni, G., and R. E. Abercrombie (2023). Investigating spectral estimates of stress drop for small to moderate earthquakes with heterogeneous slip distribution: Examples from the 2016-2017 Amatrice earthquake sequence, *J. Geophys. Res.* **128,** e2022JB025022, doi: 10.1029/2022JB025022.

Calderoni, G., and R. E. Abercrombie (2024). Combining two distinct methods to resolve spatial variation in attenuation and earthquake source parameters, *Bull. Seismol. Soc. Am.* doi: 10.1785/0120240160.

Calderoni, G., A. Rovelli, and R. Di Giovambattista (2019). Stress drop, apparent stress, and radiation efficiency of clustered earthquakes in the nucleation volume of the 6 April 2009, M_w 6.1 L'Aquila earthquake, *J. Geophys. Res.* **124,** 10,360–10,375, doi: 10.1029/2019JB017513.

California Geological Survey (1972). *California Strong Motion Instrumentation Program* [Data set], International Federation of Digital Seismograph Networks, doi: 10.7914/b34q-bb70.

California Institute of Technology and USGS Pasadena (1926). *Southern California Seismic Network* [Data set], International Federation of Digital Seismograph Networks, doi: 10.7914/SN/CI.

Chen, X., and R. E. Abercrombie (2020). Improved approach for stress drop estimation and its application to an induced earthquake sequence in Oklahoma, *Geophys. J. Int.* **223,** 233–253, doi: 10.1093/gji/ggaa316.

Chen, X., Q. Wu, and C. Pennington (2025). Factors that influence variability in stress drop measurements using spectral decomposition and spectral ratio methods for the 2019 Ridgecrest earthquake sequence, *Bull. Seismol. Soc. Am.* doi: 10.1785/0120240150 (this issue).

Chen, X., J. Yin, C. Pennington, Q. Wu, and Z. Zhan (2025). Effect of time window and spectral measurement options on empirical green's function analysis using DAS array and seismic stations, *Bull. Seismol. Soc. Am.* doi: 10.1785/0120240156.

Chu, S., A. S. Baltay, and R. E. Abercrombie (2025). Characterizing directivity in small (M 3-5) aftershocks of the Ridgecrest sequence, *Bull. Seismol. Soc. Am.* doi: 10.1785/0120240146.

Clinton, J. E., E. Hauksson, and K. Solanki (2006). An evaluation of the SCSN moment tensor solutions: Robustness of the M_w magnitude scale, style of faulting, and automation of the method, *Bull. Seismol. Soc. Am.* **96,** 1689–1705, doi: 10.1785/0120050241.

Cochran, E. S., E. Wolin, D. E. McNamara, A. Yong, D. Wilson, M. Alvarez, N. van der Elst, A. McClain, and J. Steidl (2020). The U.S. Geological Survey's rapid seismic array deployment for the 2019 Ridgecrest earthquake sequence, *Seismol. Res. Lett.* **91,** no. 4, 1952–1960, doi: 10.1785/0220190296.

Cochran, E. S., A. Baltay, S. Chu, R. E. Abercrombie, D. Bindi, X. Chen, G. A. Parker, C. Pennington, P. M. Shearer, and D. T. Trugman (2024). SCEC/USGS community stress drop validation study: How spectral fitting approaches influence measured source parameters, *Bull. Seismol. Soc. Am.* doi: 10.1785/0120240140.

Cotton, F., R. Archuleta, and M. Causse (2013). What is sigma of the stress drop?, *Seismol. Res. Lett.* **84,** no. 1, 42–48, doi: 10.1785/0220120087.

Denolle, M. A., and P. M. Shearer (2016). New perspectives on self-similarity for shallow thrust earthquakes, *J. Geophys. Res.* **121,** 6533–6565, doi: 10.1002/2016JB013105.

Dreger, D. (1997). The large aftershocks of the Northridge earthquake and their relationship to mainshock slip and fault zone complexity, *Bull. Seismol. Soc. Am.* **87,** 1259–1266, doi: 10.1785/BSSA0870051259.

Dreger, D. S., L. Malagnini, T. Taira, and J. Magana (2021). Comparing finite-source and corner frequency based stress drop for the Ridgecrest sequence, *Annual Meeting of American Geophysical Union*, S45A-0288.

Eulenfeld, T. (2024). Qopen Ridgecrest, doi: 10.5281/zenodo.11487772.

Eulenfeld, T., and U. Wegler (2016). Measurement of intrinsic and scattering attenuation of shear waves in two sedimentary basins and comparison to crystalline sites in Germany, *Geophys. J. Int.* **205,** no. 2, 744–757, doi: 10.1093/gji/ggw035.

Eulenfeld, T., T. Dahm, S. Heimann, and U. Wegler (2021). Fast and robust earthquake source spectra and moment magnitudes from envelope inversion, *Bull. Seismol. Soc. Am.* doi: 10.1785/0120210200.

Eulenfeld, T., G. Hillers, T. A. T. Vuorinen, and U. Wegler (2023). Induced earthquake source parameters, attenuation, and site effects from waveform envelopes in the Fennoscandian Shield, *J. Geophys. Res.* **128,** no. 4, e2022jb025162, doi: 10.1029/2022jb025162.

Hanks, T. C. (1979). b values and $\omega^{-\gamma}$ seismic source models: Implications for tectonic stress variations along active crustal fault zones and the estimation of high-frequency strong ground motion, *J. Geophys. Res.* **84,** 2235–2241, doi: 10.1029/JB084iB05p02235.

Hanks, T. C. (1981). The corner frequency shift, earthquake source models, and Q, *Bull. Seismol. Soc. Am.* **71,** no. 3, 597–612, doi: 10.1785/BSSA0710030597.

Hanks, T. C., and H. Kanamori (1979). A moment magnitude scale, *J. Geophys. Res.* **84,** no. B5, 2348–2350, doi: 10.1029/JB084iB05p02348.

Hanks, T. C., and M. Wyss (1972). The use of body-wave spectra in the determination seismic-source parameters, *Bull. Seismol. Soc. Am.* **62,** 569–589.

Huang, Y., G. C. Beroza, and W. L. Ellsworth (2016). Stress drop estimates of potentially induced earthquakes in the Guy-Greenbrier sequence, *J. Geophys. Res.* **121,** no. 9, 6597–6607.

Huang, Y., W. L. Ellsworth, and G. C. Beroza (2017). Stress drops of induced and tectonic earthquakes in the central United States are indistinguishable, *Sci. Adv.* **3,** no. 8, e1700772, doi: 10.1126/sciadv.1700772.

Ji, C., R. Archuleta, and A. Peyton (2024). Capturing broadband spectral characteristics of moderate-size earthquakes using nearby recordings: A case study of 42 M_w 4.0–5.4 Ridgecrest earthquakes, *Bull. Seismol. Soc. Am.* doi: 10.1785/0120240180.

Kaneko, Y., and P. M. Shearer (2015). Variability of seismic source spectra, estimated stress drop, and radiated energy, derived from cohesive-zone models of symmetrical and asymmetrical circular and elliptical ruptures, *J. Geophys. Res.* **120,** 1053–1079, doi: 10.1002/2014JB011642.

Kemna, K. B., A. Verdecchia, and R. M. Harrington (2021). Spatiotemporal evolution of earthquake static stress drop values in the 2016–2017 central Italy seismic sequence, *J. Geophys. Res.* **126,** e2021JB022566, doi: 10.1029/2021JB022566.

Kempton, J. J., and J. P. Stewart (2006). Prediction equations for significant duration of earthquake ground motions considering site and near-source effects, *Earthq. Spectra* **22,** no. 4, 985–1013, doi: 10.1193/1.2358175.

Kennett, B. L. N., and E. R. Engdahl (1991). Travel times for global earthquake location and phase association. *Geophys. J. Int.* **105,** 429–465, doi: 10.1111/j.1365-246X.1991.tb06724.x.

Klimasewski, A., V. Sahakian, A. Baltay, J. Boatwright, J. B. Fletcher, and L. Baker (2019). $\kappa 0$ and broadband site spectra in Southern California from source model-constrained inversion, *Bull. Seismol. Soc. Am.* **109,** no. 5, 1878–1889, doi: 10.1785/0120190037.

Knudson, T. C., W. L. Ellsworth, and G. C. Beroza (2025). Source parameter analysis using maximum amplitudes in the time domain. *Bull. Seismol. Soc. Am.* doi: 10.1785/0120240198.

Lior, I., and A. Ziv (2017). The relation between ground acceleration and earthquake source parameters: Theory and observations, *Bull. Seismol. Soc. Am.* **107,** no. 2, 1012–1018, doi: 10.1785/0120160251.

Liu, M., Y. Huang, and J. Ritsema (2020). Stress drop variation of deep-focus earthquakes based on empirical Green's functions, *Geophys. Res. Lett.* **47,** no. 9, e2019GL086055, doi: 10.1029/2019GL086055.

Madariaga, R. (1976). Dynamics of an expanding circular fault, *Bull. Seismol. Soc. Am.* **66,** no. 3, 639–666, doi: 10.1785/BSSA0660030639.

Mayeda, K., D. Bindi, J. Roman-Nieves, P. Morasca, D. Dreger, C. Ji, T. Taira, R. Archuleta, W. Walter, and J. Barno (2024). Source scaling comparison and validation for Ridgecrest, CA: Radiated energy, apparent stress, and M_w using the coda calibration tool ($2.6 < M_w < 7.1$), *Bull. Seismol. Soc. Am.* doi: 10.1785/0120240143.

Mayeda, K., A. Hofstetter, J. L. O'Boyle, and W. R. Walter (2003). Stable and transportable regional magnitudes based on coda-derived moment rate spectra, *Bull. Seismol. Soc. Am.* **93,** 224–239, doi: 10.1785/0120020020.

Mori, J., and S. Hartzell (1990). Source inversion of the 1988 Upland, California earthquake: Determination of a fault plane for a small event, *Bull. Seismol. Soc. Am.* **80,** 507–518, doi: 10.1785/BSSA0800030507.

Nakano, K., S. Matsushima, and H. Kawase (2015). Statistical properties of strong ground motions from the generalized spectral inversion of data observed by K-NET, KiK-net, and the JMA Shindokei network in Japan, *Bull. Seismol. Soc. Am.* **105,** no. 5, 2662–2680, doi: 10.1785/0120140349.

Oth, A., D. Bindi, S. Parolai, and D. Di Giacomo (2011). Spectral analysis of K-NET and KiK-net data in Japan, part II: On attenuation characteristics, source spectra, and site response of borehole and surface stations, *Bull. Seismol. Soc. Am.* **101,** no. 2, 667–687, doi: 10.1785/0120100135.

Parker, G., A. Baltay, J. Rekoske, and E. M. Thompson (2020). Repeatable Source-, Path-, and Site-Effects from the 2019 Ridgecrest M 7.1 Earthquake Sequence, *Bull. Seismol. Soc. Am.* **110,** 1530–1548, doi: 10.1785/0120200008.

Pennington, C. N., X. Chen, R. E. Abercrombie, and Q. Wu (2021). Cross validation of stress drop estimates and interpretations for the 2011 Prague, OK, earthquake sequence using multiple methods, *J. Geophys. Res.* **126,** e2020JB020888, doi: 10.1029/2020JB020888.

Prieto, G. A. (2022). The multitaper spectrum analysis package in Python, *Seismol. Res. Lett.* **93,** 1922–1929, doi: 10.1785/0220210332.

Rekoske, J., E. Thompson, M. Moschetti, M. Hearne, B. Aagaard, and G. A. Parker (2020). The 2019 Ridgecrest, California, earthquake sequence ground motions: Processed records and derived intensity metrics, *Seismol. Res. Lett.* **91,** no. 4, 2010–2023, doi: 10.1785/0220190292.

Rekoske, J., E. M. Thompson, M. P. Moschetti, M. Hearne, B. T. Aagaard, and G. A. Parker (2019). Ground motions from the 2019 Ridgecrest, California, earthquake sequence, *Center for Engineering Strong Motion Data (CESMD)*, doi: 10.5066/P9REBW60.

Ripperger, J., and P. M. Mai (2004). Fast computation of static stress changes on 2D faults from final slip distributions, *Geophys. Res. Lett.* **31,** L18610, doi: 10.1029/2004GL020594.

Sato, T., and T. Hirasawa (1973). Body wave spectra from propagating shear cracks, *J. Phys. Earth* **21,** no. 4, 415–431.

Satriano, C. (2024). SourceSpec – Earthquake source parameters from P- or S-wave displacement spectra (v1.8), doi: 10.5281/ZENODO.3688587.

Satriano, C., A. R. Mejia Uquiche, and J. M. Saurel (2016). Spectral estimation of seismic moment, corner frequency and radiated energy for earthquakes in the Lesser Antilles, *AGU Fall Meeting Abstracts*, Vol. 2016, pp. S13A-2518, bibcode: 2016AGUFM.S13A2518S.

Southern California Earthquake Center (SCEDC) (2013). *Southern California Earthquake Center, Caltech*, Dataset, doi: 10.7909/C3WD3xH1.

Shearer, P. M., and R. E. Abercrombie (2021). Calibrating spectral decomposition of local earthquakes using borehole seismic records—Results for the 1992 Big Bear aftershocks in southern California, *J. Geophys. Res.* **126,** e2020JB020561.

Shearer, P. M., R. E. Abercrombie, and D. T. Trugman (2022). Improved stress drop estimates for M 1.5 to 4 earthquakes in southern California from 1996 to 2019, *J. Geophys. Res.* **127,** doi: 10.1029/2022JB024243.

Shearer, P. M., R. E. Abercrombie, D. T. Trugman, and W. Wang (2019). Comparing EGF methods for estimating corner frequency and stress drop from P wave spectra, *J. Geophys. Res.* **124,** 3966–3986, doi: 10.1029/2018JB016957.

Shearer, P. M., G. A. Prieto, and E. Hauksson (2006). Comprehensive analysis of earthquake source spectra in southern California, *J. Geophys. Res.* **111,** no. B06303, doi: 10.1029/2005JB003979.

Shearer, P. M., I. Vandevert, W. Fan, R. E. Abercrombie, D. Bindi, G. Calderoni, X. Chen, W. Ellsworth, R. Harrington, Y. Huang, *et al.* (2024). Earthquake source spectra estimates vary widely for two Ridgecrest aftershocks because of differences in attenuation corrections, *Bull. Seismol. Soc. Am.* doi: 10.1785/0120240134.

Supino, M., G. Festa, and A. Zollo (2019). A probabilistic method for the estimation of earthquake source parameters from spectral inversion: application to the 2016–2017 Central Italy seismic sequence, *Geophys. J. Int.* **218,** no. 2, 988–1007, doi: 10.1093/gji/ggz206.

Supino, M., L. Scognamiglio, L. Chiaraluce, C. Doglioni, and A. Herrero (2024). Source characterization of the 20th May 2024 MD 4.4 Campi Flegrei caldera earthquake through a joint source-propagation probabilistic inversion, *Seismica* **3,** no. 2, doi: 10.26443/seismica.v3i2.1394.

Thatcher, W., and T. C. Hanks (1973). Source parameters of southern California earthquakes, *J. Geophys. Res.* **78,** no. 35, 8547–8576, doi: 10.1029/JB078i035p08547.

Thompson, E. M., M. Hearne, B. T. Aagaard, J. M. Rekoske, C. B. Worden, M. P. Moschetti, H. E. Hunsinger, G. C. Ferragut, G. A. Parker, J. A. Smith, *et al.* (2024a). USGS automated ground motion processing software version 2, *U.S. Geol. Surv. Software Release*, doi: 10.5066/P13HMKFJ.

Thompson, E. M., M. Hearne, B. T. Aagaard, J. M. Rekoske, C. B. Worden, M. P. Moschetti, H. E. Hunsinger, G. C. Ferragut, G. A. Parker, J. A. Smith, *et al.* (2024b). Automated, near real-time ground-motion processing at the U.S. Geological Survey, *Seismol. Res. Lett.* doi: 10.1785/0220240021 (in review).

Trugman, D. T. (2020). Stress-drop and source scaling of the 2019 Ridgecrest, California, earthquake sequence, *Bull. Seismol. Soc. Am.* **110,** 1859–1871, doi: 10.1785/0120200009.

Trugman, D. T., and P. M. Shearer (2017). Application of an improved spectral decomposition method to examine earthquake source scaling in Southern California, *J. Geophys. Res.* **122,** 2890–2910, doi: 10.1002/2017JB013971.

University of Nevada, Reno (1971). *Nevada Seismic Network* [Data set], International Federation of Digital Seismograph Networks, doi: 10.7914/SN/NN.

University of Nevada, Reno (1992). *Southern Great Basin Network* [Data set], International Federation of Digital Seismograph Networks, doi: 10.7914/SN/SN.

U.S. Geological Survey (1931). *United States National Strong-Motion Network* [Data set], International Federation of Digital Seismograph Networks, doi: 10.7914/SN/NP.

Vandevert, I., P. M. Shearer, and W. Fan (2024). Ridgecrest aftershock stress drops from P- and S-wave spectral decomposition, *Bull. Seismol. Soc. Am.* doi: 10.1785/0120240133.

Yenier, E., and G. M. Atkinson (2015). Regionally adjustable generic ground-motion prediction equation based on equivalent point-source simulations: Application to Central and Eastern North America, *Bull. Seismol. Soc. Am.* **105,** 1989–2009, doi: 10.1785/0120140332.

Yoshimitsu, N., W. L. Ellsworth, and G. C. Beroza (2019). Robust stress drop estimates of potentially induced earthquakes in Oklahoma: Evaluation of empirical Green's function, *J. Geophys. Res.* **124,** 5854–5866, doi: 10.1029/2019JB017483.

Zhang, J., and H. Yang (2025). Improved source parameter estimation of earthquakes in the 2019 Ridgecrest sequence based on a global-optimization algorithm and their implications on fault behaviors, *Bull. Seismol. Soc. Am.* doi: 10.1785/0120240111.

Zhang, J., H. Yang, J. Zi, J. Su, and X. Chen (2024). An improved estimation of stress drop and its application on induced earthquakes in the Weiyuan Shale Gas Field in China, *Geophys. J. Int.* **236,** no. 3, 1785–1803, doi: 10.1093/gji/ggae014.

AUTHORS AND AFFILIATIONS

Rachel E. Abercrombie: Department of Earth and Environment, Boston University, Boston, Massachusetts, U.S.A., https://orcid.org/0000-0003-4515-5420; **Annemarie Baltay:** U.S. Geological Survey, Earthquake Science Center, Moffett Field, California, U.S.A., https://orcid.org/0000-0002-6514-852X; **Shanna Chu:** Department of Earth, Environmental, and Planetary Sciences, Rice University, Houston, Texas, U.S.A., https://orcid.org/0000-0001-5974-183X; **Taka'aki Taira:** Berkeley Seismological Laboratory, UC Berkeley, Berkeley, California, U.S.A., https://orcid.org/0000-0002-6170-797X; **Dino Bindi:** German Research Centre for Geoscience GFZ, Potsdam, Germany, https://orcid.org/0000-0002-8619-2220; **Oliver S. Boyd:** U.S. Geological Survey, Geologic Hazards Science Center, Golden, Colorado, U.S.A., https://orcid.org/0000-0001-9457-0407; **Xiaowei Chen:** Department of Geology and Geophysics, Texas A&M University, College Station, Texas, U.S.A., https://orcid.org/0000-0001-6362-3297; **Elizabeth S. Cochran:** U.S. Geological Survey, Earthquake Science Center, Pasadena, California, U.S.A., https://orcid.org/0000-0003-2485-4484; **Emma Devin:** Department of Astrophysical Sciences, Princeton University, Princeton, New Jersey, U.S.A., https://orcid.org/0000-0003-4657-1530; **Douglas Dreger:** University of California, Berkeley, California, U.S.A., https://orcid.org/0000-0002-6590-3089; **William Ellsworth:** Department of Geophysics, Stanford University, Stanford, California, U.S.A., https://orcid.org/0000-0001-8378-4979; **Wenyuan Fan:** Scripps Institution of Oceanography, University of California San Diego, La Jolla, California, U.S.A., https://orcid.org/0000-0002-2983-8240; **Rebecca M. Harrington:** Institute of Geology, Mineralogy, and Geophysics, Ruhr University Bochum, Germany, https://orcid.org/0000-0002-3538-8020; **Yihe Huang:** Department of Earth and Environmental Sciences, University of Michigan, Ann Arbor, Michigan, U.S.A., https://orcid.org/0000-0001-5270-9378; **Kilian B. Kemna:** Institute of Geology, Mineralogy, and Geophysics, Ruhr University Bochum, Germany, https://orcid.org/0000-0001-6160-5079; **Meichen Liu:** Division of Geological and Planetary Sciences, California Institute of Technology, Pasadena, California, U.S.A., https://orcid.org/0000-0001-7952-340X; **Adrien Oth:** European Center for Geodynamics and Seismology, Walferdange, Luxembourg, https://orcid.org/0000-0003-4859-6504; **Grace A. Parker:** U.S. Geological Survey, Earthquake Science Center, Moffett Field, California, U.S.A., https://orcid.org/0000-0002-9445-2571; **Colin Pennington:** Lawrence Livermore National Laboratory, Livermore, California, U.S.A., https://orcid.org/0000-0002-1474-9368; **Matteo Picozzi:** National Institute of Oceanography and Applied Geophysics OGS, Trieste, Italy, https://orcid.org/0000-0001-8078-9416; **Christine J. Ruhl:** Verisk Analytics, Boston, Massachusetts, U.S.A., https://orcid.org/0000-0002-7764-3165; **Peter Shearer:** Scripps Institution of Oceanography, University of California San Diego, La Jolla, California, U.S.A., https://orcid.org/0000-0002-2992-7630; **Daniele Spallarossa:** Department for Earth, Environment and Life Sciences DISTAV, University of Genoa, Genoa, Italy, https://orcid.org/0000-0002-8021-3908; **Daniel Trugman:** Nevada Seismological Laboratory, Nevada Geosciences, University of Nevada, Reno, Nevada, U.S.A., https://orcid.org/0000-0002-9296-4223; **Ian Vandevert:** Scripps Institution of Oceanography, University of California San Diego, La Jolla, California, U.S.A., https://orcid.org/0000-0001-9560-4787; **Qimin Wu:** Lettis Consultants International, Inc., Concord, California, U.S.A., https://orcid.org/0000-0001-8315-8388; **Clara Yoon:** U.S. Geological Survey, Earthquake Science Center, Pasadena, California, U.S.A., https://orcid.org/0000-0003-4521-3889; **Ellen Yu:** Southern California Earthquake Data Center, Caltech Seismological Laboratory, Pasadena, California, U.S.A., https://orcid.org/0000-0002-2480-8384; **Gregory C. Beroza:** Department of Geophysics, Stanford University, Stanford, California, U.S.A., https://orcid.org/0000-0002-8667-1838; **Tom Eulenfeld:** Friedrich Schiller University Jena, Germany, https://orcid.org/0000-0002-8378-559X; **Trey Knudson:** Department of Geophysics, Stanford University, Stanford, California, U.S.A., https://orcid.org/0009-0007-0350-5732; **Kevin Mayeda:** Air Force Technical Applications Center, Patrick Space Force Base, Florida, U.S.A., https://orcid.org/0000-0003-0980-0605; **Paola Morasca:** Istituto Nazionale di Geofisica e Vulcanologia, INGV, Milan, Italy, https://orcid.org/0000-0002-6525-4867; **James S. Neely:** Department of the Geophysical Sciences, University of Chicago, Chicago, Illinois, U.S.A., https://orcid.org/0000-0003-4029-2979; **Jorge Roman-Nieves:** Air Force Technical Applications Center, Patrick Space Force Base, Florida, U.S.A., https://orcid.org/0009-0001-8657-3920; **Claudio Satriano:** Université Paris Cité, Institut de physique du globe de Paris, CNRS, Paris, France, https://orcid.org/0000-0002-3039-2530; **Mariano Supino:** Istituto Nazionale di Geofisica e Vulcanologia, Osservatorio Nazionale Terremoti, Rome, Italy, https://orcid.org/0000-0002-7222-9344; **William R. Walter:** Lawrence Livermore National Laboratory, Livermore, California, U.S.A., https://orcid.org/0000-0002-0331-0616; **Ralph Archuleta:** Department of Earth Science, University of California, Santa Barbara, California, U.S.A., https://orcid.org/0000-0003-4902-5412; **Gail Marie Atkinson:** University of Western Ontario London, Ontario, Canada, https://orcid.org/0000-0003-2403-1349; **Giovanna Calderoni:** Istituto Nazionale di Geofisica e Vulcanologia, Rome, Italy, https://orcid.org/0000-0002-3712-4432; **Chen Ji:** Department of Earth Science, University of California, Santa Barbara, California, U.S.A., https://orcid.org/0000-0002-0350-5704; **Hongfeng Yang:** Department of Earth and Environmental Sciences, The Chinese University of Hong Kong, Hong Kong, China, https://orcid.org/0000-0002-5925-6487; and **Jiewen Zhang:** Department of Earth and Environmental Sciences, The Chinese University of Hong Kong, Hong Kong, China, https://orcid.org/0000-0001-8130-9453

Manuscript received 3 July 2024
Published online 2 May 2025